Hydrodynamics of Gas–Liquid Slug Flows in a Long In-Plane Spiral Shaped Milli-Reactor[1]

Mei Mei[a, b, c], Francisco Felis[b, c], Gilles Hébrard[a], Nicolas Dietrich[a], and Karine Loubière[b, *

[a]*Toulouse Biotechnology Institute Bio and Chemical Engineering (TBI), Université de Toulouse, CNRS, INRAE, INSA, Toulouse, France*

[b]*Laboratoire de Génie Chimique (LGC), Université de Toulouse, CNRS, INPT, UPS, Toulouse, France*

[c]*FR FERMaT, Université de Toulouse, CNRS, INPT, INSA, UPS, Toulouse, France*

**e-mail: Karine.loubiere@ensiacet.fr*

Abstract—An experimental investigation of gas–liquid Taylor flows in a millimetric in-plane spiral shaped reactor with various tube curvature ratios ($52 < \lambda < 166$) is reported. Thanks to the compactness of the reactor and the use of an ad hoc imaging system and processing, the axial evolution of bubble lengths and velocities could be recorded and extracted along the whole reactor length (~3 m). The experimental results showed a significant linear increase of bubble length and velocity with axial position. Very long, stable Taylor bubbles (L_B/d_{it} up to 40) and liquid slugs were generated, in particular due to the poor wettability of the surface and the important role it played in bubble formation. At identical inertial force (i.e., identical Reynolds number), a higher centrifugal force (i.e., lower tube curvature ratio) likely led to shorter Taylor bubble lengths while only slightly affecting the liquid slug lengths. The axial pressure drop could be estimated from the axial increase in bubble volume, and compared with the measured pressure drop and that predicted by the correlations from literatures. By considering both the friction and capillary pressure drops, it was observed that the predicted two-phase pressure drop was slightly dependent on the centrifugal force and that the capillary pressure drop, determined from the unit cell number, capillary number and static contact angle, was dominant.

INTRODUCTION

Gas–liquid reactive bubbly flows occupy a central place in a broad range of processes used in industries such as petrochemicals, cosmetics, mineral processing and wastewater treatment, and in many chemical and biochemical processes. However, the mass transfer between phases is often the limiting step for implementing chemical reactions with high yield and selectivity. This is the case, for example, in the fine chemistry and pharmaceutical industries, for catalytic hydrogenations, sensitized photo-oxygenations, photo-redox reactions, or fluorinations [1−3]. With respect to safety, compactness, quality and eco-impact issues, some cutting-edge technologies for process intensification, such as continuous-flow micro-structured technologies (heat-exchanger-reactor, monolith reactor, micro-reactor, etc.), have emerged as alternatives to conventional equipment (e.g. batch processing). They usually involve confined configurations, such as micro/milli tubes/channels, offering enhanced heat and mass transfer, efficient mixing, and high exchange surface areas [4−7].

Among all the gas–liquid flow patterns in micro- or milli-channels, Taylor flow is one of the most widely investigated flow regimes as it provides stable, regular and easily tunable conditions with enhanced heat and mass transfer efficiencies. Curved geometries, such as meandering channels [8], helically coiled tubes [9], spiral shaped tubes [10] or tubes with bends [11] have been widely adopted for the design of miniaturized reactors [12] because they provide: (i) efficient cross-sectional mixing; (ii) intensified mass transfer and heat transfer and (iii) increased compactness and narrow residence time distribution. The in-plane spiral shaped reactors, recently applied for photochemical reactions [10, 13, 14], offer an alternative meandering design: the curvature changes along the channel length while remaining in the same plane. Most previous works related to curved geometries have focused on single phase flows [15], separating particles [16] and mixing [17]. Surprisingly, little attention has been paid to the gas–liquid hydrodynamics and mass transfer characteristics of gas–liquid Taylor flow inside such geometries.

Table 1. Geometrical parameters related to the Archimedean spiral

Spiral shape	D_{SR}, mm	n_{SR}	P_{SR}, mm	L_{SR}, mm
SR	5	19.25	4	2.95

Some recent reviews [18, 19] and studies [20, 21] have thoroughly reported the hydrodynamics and mass transfer characteristics of gas−liquid Taylor flow in micro- or milli-channels. The influence of bends (either return bends or continuous curvature) on the gas−liquid Taylor flow hydrodynamics in micro-channels has been pointed out by several authors [17, 22−24]. Due to the centrifugal force, secondary flows (Dean vortices) are generated in the cross-sectional area of the curved channel, and the symmetrical recirculation loops in the liquid slugs observed in a straight channel then become asymmetrical. Muradoglu et al. [24] made a numerical study of the motion of gas bubbles in curved channels and found that the liquid lubrication film at the outer wall was thicker than the one at the inner wall. Lubrication theory predicted that the slip velocity of bubble relative to the liquid would always be higher in a curved channel than in a straight channel and would increase monotonically with channel curvature ratio (i.e. the curved channel diameter divided by the cross-sectional diameter of the channel). The gas−liquid slug flow in curved channels with various curvature ratios (5−30) was simulated numerically by Kumar et al. [23], using the volume of fluid (VOF) method for interface tracking. They pointed out that, in contrast to the situation in a straight channel, the bubble and liquid slug lengths were not only controlled by inlet geometries and by the total two-phase superficial velocities, but were also dependent on the curvature ratio. Shorter slug lengths were achieved at lower curvature ratios because of the stronger centrifugal force. The surface tension and wall surface adhesion were also found to affect the slug lengths. Kawahara et al. [25] investigated the gas−liquid flow characteristics in a micro-channel with return bends and, interestingly, observed that there was an increase of bubble length (i.e. a gas volume expansion caused by pressure drop) in the long micro-channel as the bubble flowed downstream. This study also highlighted the important effects of pressure drop (estimated at about 22−68 kPa for four bend experiments and 13−55 kPa for single bend experiments) on the gas−liquid hydrodynamic characteristics.

Compared to straight channels, curved channels with small curvature ratios [9] induced increasing pressure drops. Ide et al. [26] also reported that the pressure drop was thus pretty high (up to 1811 kPa) [27] in an extremely long micro-channel (ratio of channel length to the hydraulic diameter of tube ~1.7×10^4), and that the axial bubble length and velocity increased along the channel. Several studies have shown the important role of surface wettability in the overall pressure drops in gas−liquid Taylor flow, through experiments [28, 29], modelling [30, 31] or numerical simulation [23]. More specifically, they observed that the capillary pressure drop induced by the contact angle hysteresis (CAH) for the poorly wetting (contact angle >90°) cases was higher than the frictional pressure drop. The wettability could also change the bubble and liquid slug shape [32], and induce longer bubble and liquid slug lengths [33]. In addition, Cubaud et al. [34] investigated the liquid film of the gas−liquid flow in various hydrophilic and hydrophobic channels. They found that, unlike in hydrophilic flows, bubbles were not lubricated under hydrophobic flows and triple lines (gas/liquid/solid) were thus created.

In addition to investigations related to the gas−liquid hydrodynamics in curved reactors, various authors have shown that the gas−liquid mass transfer was enhanced by the occurrence of centrifugal force [8, 35]. Recently, Krieger et al. [36] defined a modified Dean number to describe the transition in gas−liquid flow regimes caused by the superposition of Taylor and Dean flow. Kovats et al. [37] used a colourimetric method based on indigo carmine dye to investigate the enhancement of mass transfer in a helically coiled pipe. However, the effects of a continuous change of Dean number along the channel length (as occurring in the in-plane spiral shaped reactor) on gas−liquid mass transfer have not been investigated and revealed.

In this context, the present work aims to study the gas−liquid flow hydrodynamics in a long, in-plane, spiral shaped millimetric circular reactor and, in particular, to explore the effects of a continuous change of the channel curvature. This work will constitute the preliminary step required for investigating gas−liquid mass transfer inside such a reactor. The knowledge gained on both gas−liquid hydrodynamics and mass transfer characteristics in the spiral shaped milli-reactors will finally be used to provide guidelines to optimize multiphase micro/milli-reactors [3].

EXPERIMENTAL WORK

The experimental setup is shown in Fig. 1a. The in-plane spiral shaped milli-reactor consisted of a circular Fluorinated Ethylene Propylene (FEP) tube, inserted inside a square channel carved into a flat Poly-Methyl-MethAcrylate (PMMA) plate (200 × 200 × 20 mm³) and wound according to an Archimedean spiral geometry as shown in Fig. 1b. The geometrical parameters of the Archimedean spiral are illustrated in Fig. 2a and in Table 1. The inner and outer diameters of the FEP tube (reference: 1675L, CLUZEAU INFO LABO, France) were 1 and 3 mm. In polar coordinates, the Archimedean spiral could be described by

$$r = C_1 + C_2\theta, \qquad (1)$$
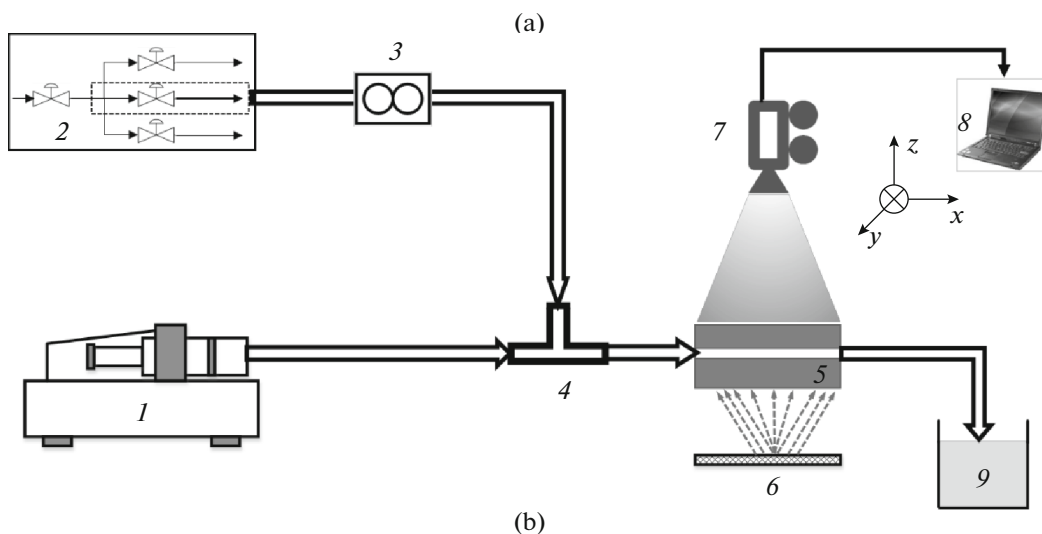
Fig. 1. (a) Schematic diagram of the experimental setup: (*1*) syringe pump; (*2*) lab air supply network; (*3*) mass flow controller; (*4*) T-junction; (*5*) spiral shaped milli-reactor; (*6*) light source; (*7*) camera; (*8*) computer; (*9*) collecting beaker. (b) Picture of the in-plane spiral shaped milli-reactor involving a typical gas−liquid Taylor flow.

where r (mm) and θ (rad) are the radial coordinate and the angular coordinate, and the coefficients C_1 and C_2 are equal to 5 mm and $2/\pi$ mm rad^{-1}, respectively.

To study the effect of the centrifugal force on the gas−liquid hydrodynamics, two configurations of tubing with identical lengths (~3 m) were investigated in this study, according to their wound positions on the plate. In this way, the intensity of the centrifugal forces could be changed while keeping the intensity of iner-

tial force constant. As shown in Fig. 2b, the first configuration corresponded to a tube wound from the 1st to the 6th spiral circles (it was named Exterior Tube and noted ET) and the second one related to a tube wound from the 7th to 15th spiral circles (named Medium Tube and noted MT). Their exact lengths were 2.97 and 2.90 m, respectively. The relative predominance of the centrifugal forces with respect to the inertial forces is classically expressed by the Dean number:
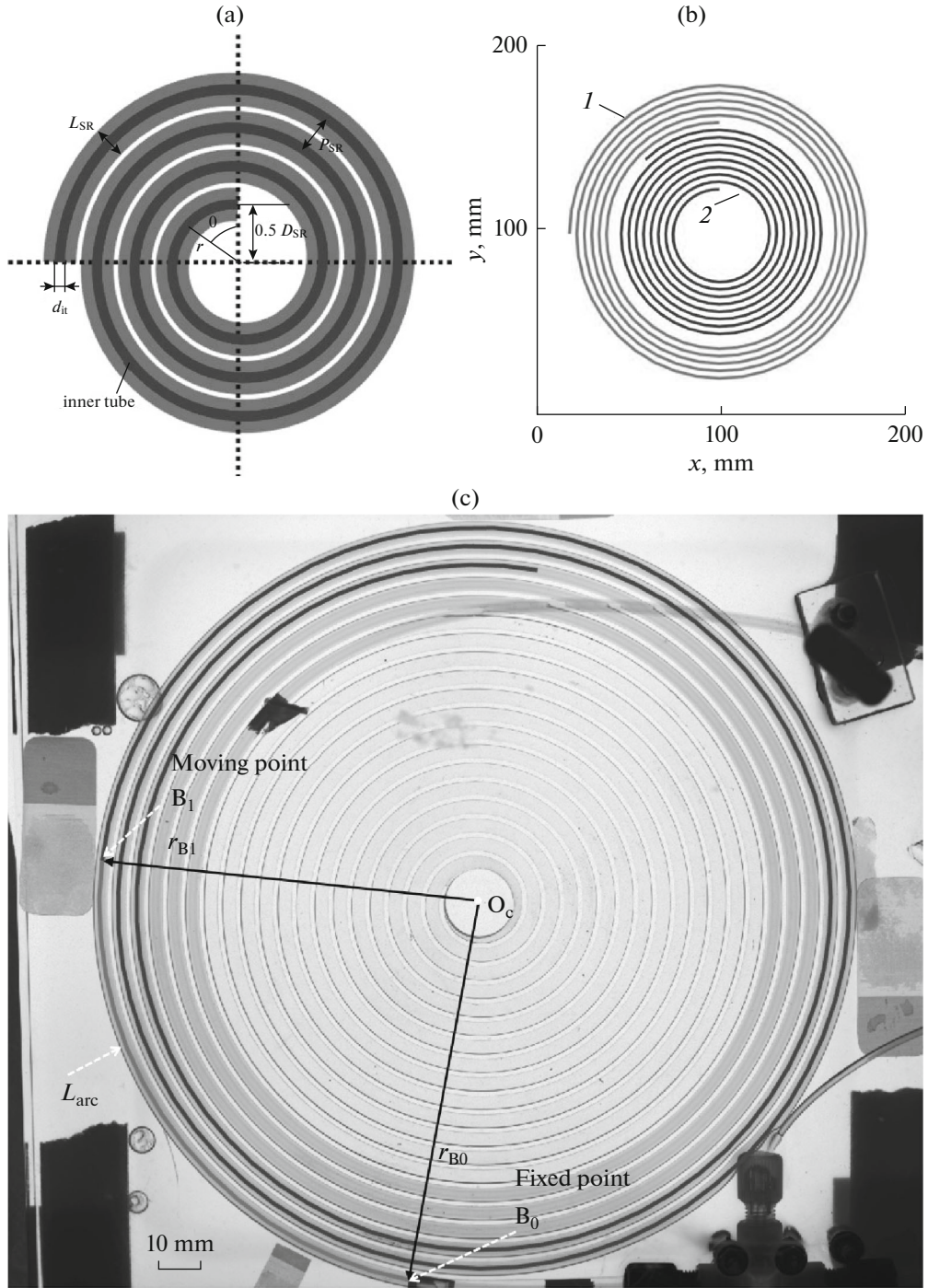
Fig. 2. (a) Geometrical parameters characteristic of the spiral shaped milli-reactor; D_{SR}, L_{SR}, P_{SR} and d_{it} are initial diameter, sectional distance, pitch distance and inner diameter of the tube, respectively. (b) Representation of the two tubing configurations: (1) Exterior Tubing (ET); (2) Medium Tubing (MT). (c) Schematic diagram used for calculating axial position; O_C refers to the spiral shaped centroid, r_{B0} and r_{B1} represent the spiral radius of a fixed point (B_0) and a moving point of the bubble centroid in the spiral curve (B_1); L_{arc} is the arc length calculated between the two points.

$$De = Re\sqrt{\frac{1}{\lambda}}, \qquad (2)$$

where λ referred to the curvature ratio, $\lambda = 2r/d_{it}$, which depended on the spiral radial radius, r, and on

the inner diameter of the tube d_{it}. The Reynolds number, Re, was defined as

$$Re = \frac{\rho_L d_{it} j_{TP}}{\mu_L}, \qquad (3)$$

Table 2. Experimental results of gas–liquid hydrodynamics in the ET configuration

j_L, cm s⁻¹	j_G, cm s⁻¹	η	$\langle U_B \rangle$, cm s⁻¹	Re_{TP}	Ca, ×10⁻⁴	$\langle De \rangle$	$\langle L_B \rangle$, mm	$\langle L_S \rangle$, mm	F_1	L_{B0}, mm	F_2, ×10⁻³, s⁻¹	U_{B0}, cm s⁻¹	p_{B0}, Pa	p_{r0}, Pa
1.80	0.82	0.45	2.70	24	3.90	2.01	6.34	8.43	0.61	5.53	0.90	2.58	134487	168830
1.80	1.08	0.60	3.02	26	4.30	2.18	7.18	6.58	0.82	6.11	1.45	2.82	141677	169733
1.80	1.37	0.76	3.30	28	4.72	2.34	8.14	5.83	1.05	6.74	2.13	3.15	148170	167588
1.80	2.79	1.55	5.28	41	6.85	3.43	12.15	4.47	1.11	10.45	2.96	4.62	133257	162940
1.80	5.13	2.85	8.63	63	10.33	5.27	18.92	3.58	1.31	16.27	4.13	7.34	125524	149822
1.80	6.87	3.81	10.32	78	12.92	6.53	22.83	3.05	1.70	20.51	5.69	9.21	126237	144025
1.80	12.69	7.05	16.89	130	21.61	10.88	33.67	2.48	1.82	31.11	7.42	15.2	118901	135512
1.80	16.60	9.22	21.78	165	27.43	13.81	40.35	2.18	1.94	37.52	8.58	19.1	116856	133886
3.61	0.87	0.24	4.23	40	6.68	3.35	5.04	12.06	0.50	4.34	1.00	4.49	135961	160701
3.61	1.12	0.31	4.48	43	7.05	3.60	5.38	10.43	0.59	4.61	1.43	4.67	139805	165664
3.61	3.04	0.84	7.21	60	9.91	5.02	8.39	5.01	1.02	7.00	4.43	6.56	145140	164855
3.61	9.30	2.58	15.12	116	19.24	9.71	15.10	3.05	1.18	13.49	8.13	13.28	127617	149098
3.61	16.02	4.44	23.19	176	29.26	14.73	21.25	2.41	1.43	19.35	11.84	20.05	123534	142254
7.22	0.91	0.13	7.41	73	12.12	6.11	4.19	19.56	0.33	3.75	0.80	8.28	127776	156640
7.22	1.41	0.20	7.84	78	12.86	6.53	4.54	15.94	0.37	4.04	1.29	8.64	128854	162506
7.22	3.16	0.44	10.14	93	15.48	7.78	5.49	6.95	0.70	4.55	4.86	10.42	147586	172916
7.22	4.87	0.67	12.91	109	18.02	9.12	6.41	4.66	0.86	5.24	7.99	12.54	150678	177275
7.22	6.22	0.86	14.93	121	20.03	10.13	7.01	3.84	1.00	5.68	10.95	13.69	154268	174687
7.22	15.48	2.14	26.05	204	33.84	17.08	11.22	2.50	1.24	9.58	20.04	23.04	140242	159696
7.22	17.68	2.45	27.30	224	37.11	18.75	11.74	2.38	1.22	10.14	21.27	25.2	137498	158989

where j_{TP} was the two-phase superficial velocity and ρ_L, μ_L the density and dynamic viscosity of liquid, respectively.

In the experiments, the curvature ratio, λ, ranged from 124 to 166 for the ET configuration and from 52 to 116 for the MT configuration, corresponding to radial coordinates, r, from 62 to 83 mm for ET and from 26 to 58 mm for MT. Then, the associated average curvature ratios, $\langle \lambda \rangle$, for ET and MT were 145 and 84, respectively. From $\langle \lambda \rangle$ and at various Reynolds numbers, the average Dean number, $\langle De \rangle$, was calculated for each operating condition, as reported in Tables 2 and 3.

During the experiments, the entire milli-reactor was put into a glass tank filled with water to avoid optical distortion (the refractive index of FEP material being 1.34 [38], so almost equal to water's 1.33).

Flow control equipment. Air was used as the gas phase and was fed in using laboratory compressed air pipelines, the air flow rates being controlled by a HORIBASTEC airflow controller (Model: SEC-Z512MGX or SEC-7320). The tube outlet was at atmospheric pressure (no counter-pressure valve was used). The liquid phase was pumped by a neMESYS syringe pump (Model: NEM-B100-01 A) equipped with a 100 mL Harvard Instruments syringe and the liquid flow rates were regulated by a mass flow control

system (Model: NEM-B100-01 A). Liquid flow rates, Q_L, ranged from 0.85 to 3.40 mL min⁻¹ and gas flow rates, Q_G, were from 0.29 to 8.33 mL min⁻¹. The associated liquid and gas superficial velocities, noted j_L and j_G (in this paper, j_G will be systematically calculated at the inlet conditions), respectively, were defined from 1.80 to 7.22 cm s⁻¹ and 0.62 to 17.68 cm s⁻¹. The ratio of the gas and liquid superficial velocities, η, varied between 0.13 and 9.52. After changing the gas and liquid flow rates, it was necessary to wait two or three times the residence time, t_R, to achieve stable, steady two-phase flow (the residence time was approximately equal to the ratio between the tube length ($L_R = 3$ m) and the total two-phase superficial velocities j_{TP}).

Fluid properties. In this study, all the experiments were performed at atmospheric pressure (1.013×10^5 Pa) and room temperature (293.15 K). The liquid phase consisted of solutions containing D-glucose anhydrous (Fischer-Scientific, CAS 50-99-7), sodium hydroxide (VWR, CAS 1310-73-2) and resazurin (Sigma Aldrich, CAS 62758-13-8, molar mass 229.19 g mol⁻¹, purity 84%). This choice of liquid phase was motivated by the fact that this study was a preliminary work for implementing the colourimetric dye-based method proposed by Dietrich et al. [39, 40] to quantify the local gas–liquid mass transfer. The D-

Table 3. Experimental results of gas−liquid hydrodynamics in the MT configuration

| j_{L}, cm s^{-1}	j_{G}, cm s^{-1}	η	$\langle U_{\mathrm{B}} \rangle$, cm s^{-1}	$\mathrm{Re_{TP}}$	Ca, $\times 10^{-4}$	$\langle \mathrm{De} \rangle$	$\langle L_{\mathrm{B}} \rangle$, mm	$\langle L_{\mathrm{S}} \rangle$, mm	F_1	L_{B0}, mm	F_2, $\times 10^{-3}$, s^{-1}	U_{B0}, cm s^{-1}	p_{B0}, Pa	p_{r0}, Pa
1.80	0.82	0.46	2.49	24	3.91	2.78	5.18	7.83	0.71	4.31	1.35	2.34	149 694	171 884
1.80	1.09	0.61	2.91	26	4.31	3.01	5.91	6.40	0.87	4.86	1.95	2.73	153 888	172 791
1.80	3.19	1.77	5.02	45	7.44	5.21	10.10	4.06	0.84	9.07	2.95	4.76	128 507	146 634
1.80	5.32	2.96	7.94	64	10.62	7.41	15.59	3.53	1.21	14.09	4.57	7.56	126 528	139 711
1.80	7.14	3.97	10.12	80	13.33	9.26	19.88	3.23	1.30	18.25	5.09	9.74	122 226	135 952
1.80	17.13	9.52	22.43	170	28.22	19.68	35.12	2.26	1.34	33.26	6.90	21.46	113 136	130 983
3.61	0.90	0.25	4.08	40	6.72	4.63	3.87	12.63	0.39	3.39	1.04	3.88	135 097	162 738
3.61	1.37	0.38	4.62	45	7.43	5.21	4.77	8.94	0.70	3.91	2.45	4.39	153 893	171 667
3.61	9.33	2.58	14.07	116	19.28	13.43	12.95	3.33	1.13	11.56	9.12	12.99	130 016	148 257
3.61	12.37	3.43	18.18	144	23.82	16.67	15.50	2.86	1.18	14.05	10.39	16.95	125 972	144 012
3.61	16.29	4.51	22.93	179	29.67	20.72	18.28	2.47	1.27	16.68	12.40	21.78	123 667	141 446
7.22	3.30	0.46	10.16	94	15.67	10.88	4.91	7.68	0.55	4.24	4.28	9.60	139 407	170 905
7.22	6.24	0.86	13.99	121	20.07	14.01	6.57	4.72	0.99	5.36	11.53	12.67	155 560	171 764
7.22	11.53	1.60	20.45	168	27.95	19.45	8.40	3.39	1.06	7.10	17.21	18.61	145 159	167 643
7.22	15.37	2.13	25.63	203	33.67	23.50	9.58	2.85	1.16	8.14	21.90	22.76	143 164	160 046

glucose anhydrous and sodium hydroxide were both diluted at 20 g L^{-1} in deionized water while the concentration of resazurin was equal to 0.105 g L^{-1}. The physical-chemical properties of the solutions measured by Dietrich et al. and Yang et al. [8, 39] at a slightly lower concentration (0.117 g L^{-1}) and at room temperature (293.15 K) were considered in this study: the density (ρ_{L}) of this solution was then 1005.3 ± 0.2 kg m^{-3}, the dynamic viscosity (μ_{L}) 1.118 ± 0.001 mPa s and the static surface tension (σ_{L}) 75.4 ± 0.5 mN m^{-1}. The apparent contact angle of the prepared solution on the FEP tubing material was measured by a Drop shape analyzer-DSA100 (Krüss) at room temperature (293.15 K). A value of 98.7 ± 0.4 was found, which was in agreement with the contact angle of 106° reported by [41] for deionized water on FEP material. This confirmed that the FEP tube remained hydrophobic for the resazurin solutions.

Image acquisition system and image processing. The gas−liquid hydrodynamics inside the in-plane spiral shaped milli-reactor was investigated by using an imaging system. The tube was lit by a Phlox-LedW-BL LED backlight (300 × 220 mm) and the images of the bubbles flowing along the tube were recorded by a 16-bit sCMOS PCO Edge camera. The acquisition time (i.e., the time interval between two consecutive images) was fixed at 0.02 s and the exposure time was 0.5 ms. The image resolution was 2560 × 2160 px^2. The camera was equipped with a Nikon AF micro Nikkor f/2.8 lens (50 mm for ET and 60 mm for MT). The regions of interest were dependent on the configurations, 197.99 × 167.05 mm^2 (ET) and 138.53 × 116.75 mm^2 (MT), so 77.3 µm (ET) and 54.0 µm (MT) for one pixel.

Before the T-junction (ref. P-633-01 from Cluzeau Info Labo®; inner diameter of 1.25 mm), the inner diameters of the gas and the liquid inlet tubing were 0.5 and 1 mm. After the T-junction where the bubbles were generated, shown in Fig. 1b, the gas−liquid flow was recorded over a large range of axial locations, noted X, from 0.25 to 2.50 m (ET and MT). Note that $X = 0$ represented the bubble formation point (i.e., T-junction). A typical raw image of the gas−liquid flow in ET is shown in Fig. 1b. All the flow patterns were recorded after several minutes (at least twice the residence time) to make sure that steady-state conditions had been achieved.

In order to extract the hydrodynamic parameters (bubble and liquid lengths, bubble velocity and void fraction, etc.) from the raw image, an image post-treatment algorithm was implemented in MATLAB® software (R2017b). First, two groups of background images were acquired: in the first one, shown in Fig. 3a, the tube was filled with the solution without resazurin (colourless) and, in the second one, shown in Fig. 3b, with the solution with resazurin and previously saturated with oxygen (pink colour). Then, the background division approach was used to extract the inner tube from the background. The tube mask image was obtained by dividing the background image when the tube was filled with saturated dye solution (Fig. 3b), by the one filled with colourless solution (Fig. 3a). By subtracting this inner-tube mask (Fig. 3c) from the raw image, only gas−liquid flow inside the tube would be accurately left on the image and other noises were eliminated efficiently.

Gas bubble detection was generated by combining the multilevel threshold based on Otsu's method [42]
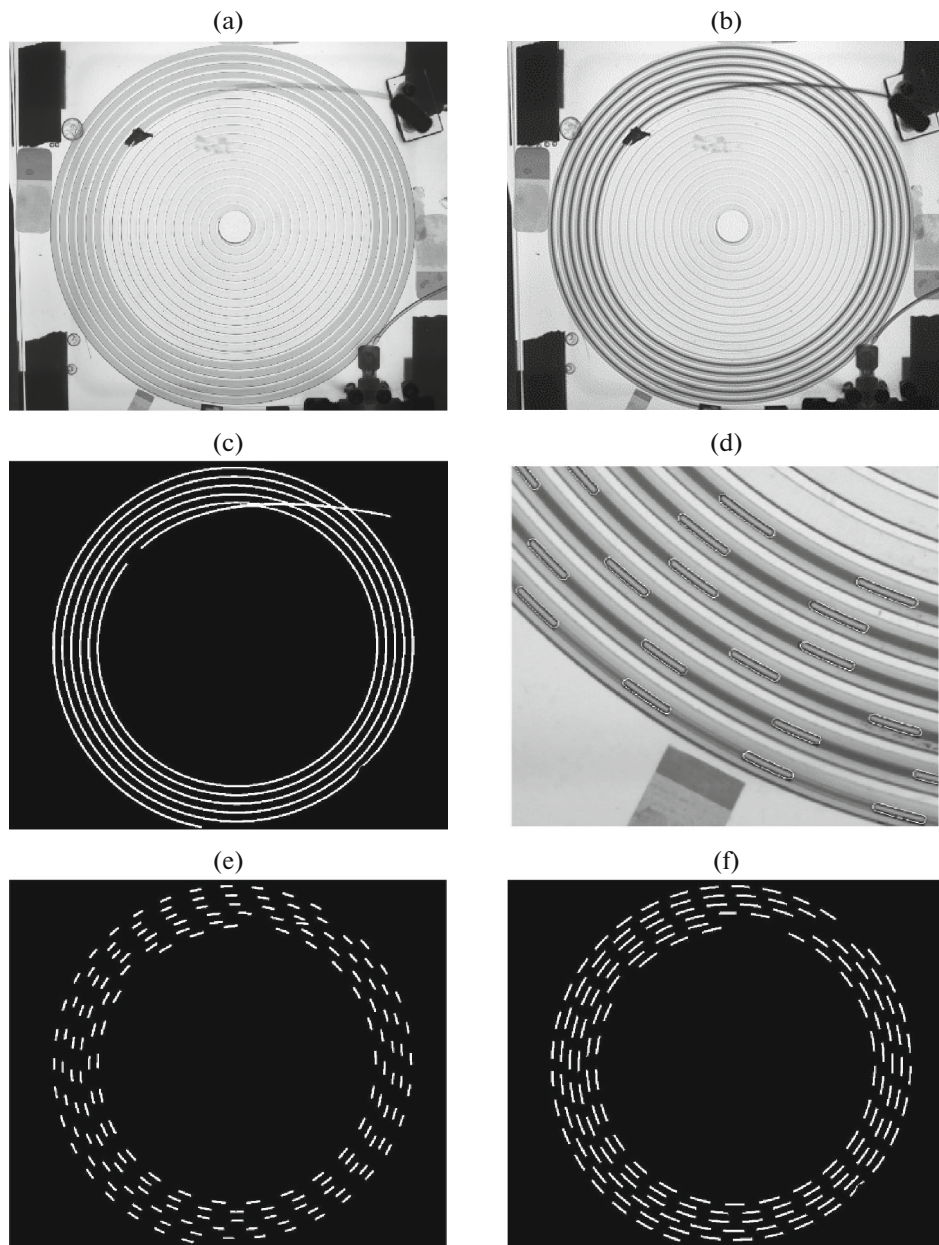
Fig. 3. (a) Raw image of the tube filled with colourless solution without resazurin. (b) Raw image of the tube filled with oxygen-saturated solution with resazurin (pink). (c) Inner-tube mask. (d) Comparison of extracted bubble edges overlapping the original image (white line represents extracted bubble edge). (e) Detection of bubbles. (f) Detection of liquid slugs.

and Canny edge detection. Specifically, the image obtained after subtraction of the tube mask from the raw image (Fig. 3c), only the gas−liquid flow remained (not shown here). Taking advantage of the significant difference between the grey intensities in the bubble inner part (high) and in the liquid slug part (low), the multilevel threshold was first applied to obtain a bubble mask. This resulted in all of the bubbles being left on the image, and roughly eliminated the liquid part. Then the Canny edge detection method was further used to accurately extract bubble edges.

Figure 3d presents an example of the extracted bubble edges (white) superimposed on the original raw image, which shows a good accuracy and confirms the efficiency of this method. Then, the liquid slug image (Fig. 3f) was acquired by subtracting the bubble image from the tube mask (Fig. 3c). This image processing made it possible to accurately detect all the bubbles and liquid slugs inside the tube, as displayed in Figs. 3e and 3f, respectively.

Gas−liquid hydrodynamic characteristics. After detecting the bubble and liquid slug images, an algo-

rithm to extract the hydrodynamic characteristics for Taylor flows was written using MATLAB® and the Image Processing Toolbox package. The characteristics concerned were bubble lengths, bubble velocity and liquid slug lengths averaged over the whole length of the spiral shaped tube, $\langle L_B \rangle$ (mm), $\langle U_B \rangle$ (cm/s) and $\langle L_S \rangle$ (mm), together with their variation with the axial location in the spiral shaped tube, $L_B(X)$ (mm), $U_B(X)$ (cm/s) and $L_S(X)$ (mm).

A Taylor bubble or liquid slug inside the spiral tube was described by a "curved" cylinder, i.e. as a cylinder with a curve as its main axis (in opposition to cylinders with straight line axis), in agreement with the experimental observations (see Results and Discussion). Therefore, their lengths were calculated by considering the curved centre line linking the tail to the nose of the cylinder. They were obtained from the detected area of the bubble or liquid slug divided by the tube inner diameter (i.e. d_{it}). More details are given in the Appendix. It should, however, be noted that this calculation can be assumed valid only if the liquid film has negligible thickness. Based on the correlations proposed by Bretherton et al. [43], which were applied to small capillary number (2×10^{-7} to 0.01), the liquid film was found to range from 3.5 and 15.8 µm thick in the present experiments, which could be considered as negligible (smaller than 2% of d_{it}). Note that, in this study, the minimum pixel resolution for images was 54 µm, thus preventing the values from being verified experimentally. This point will be further discussed in the section on pressure drop.

The average lengths of bubbles and liquid slugs, $\langle L_B \rangle$ and $\langle L_S \rangle$, were further averaged by considering the bubbles or liquid slugs detected in 50 images.

The bubble velocity was calculated from the distance travelled by the bubble centroid between two consecutive images, divided by the acquisition time. To find the correct distance, the closest distance (5–250 pixels), calculated from the centroid's original position in the first frame to its moving position in the second frame, was used as the selection criterion. It was systematically verified that the new bubble centroid (in the second frame) was located at a farther axial position than the initial bubble centroid (in the first frame). The mean bubble velocity, $\langle U_B \rangle$, was calculated by averaging over all the Taylor bubbles detected along the tube length at each frame and then by considering 100 image frames.

For the whole set of Taylor bubbles detected on a given image, the associated bubble lengths, $L_B(X)$, and the bubble velocities, $U_B(X)$, were initially ranked according to their radial radius, r, i.e. to the radial distance from their centroid to the centroid of the spiral shape (point O_c in Fig. 2c). To convert this radius into an axial position X, the corresponding arc length from the T-junction was determined. Eq. (4) was used to

calculate the arc length between two random points, B_0 and B_1, on the spiral curve in polar coordinates, (Fig. 2c)

$$L_{arc} = \int_{\theta_{B0}}^{\theta_{B1}} \sqrt{r^2 + \left(\frac{dr}{d\theta}\right)^2} d\theta = \int_{\theta_{B0}}^{\theta_{B1}} \sqrt{(C_1 + C_2\theta)^2 + C_2^2} d\theta, \quad (4)$$

where θ_{B0} and θ_{B1} represent the initial angle of a fixed point B_0 on the image and the moving angle of a random bubble (point B_1), which could be calculated from Equation (1) knowing that the radial radii r_{B0} and r_{B1} were derived directly from the image. This fixed point B_0 was measured and known for the distance from the bubble formation point (Fig. 2c). After calculating the arc length of any random bubble from the fixed point B_0, the axial position X could be obtained for any detected bubble. Finally, the evolution of bubble length and velocity along the axial position was found.

For any given operating conditions, the standard deviations of bubble length, liquid slug length and bubble velocity were smaller than 10%, 5% and 10%, respectively, of the average values.

RESULTS AND DISCUSSION

Flow regimes and bubble shape. The gas–liquid flow regimes can be affected by several parameters such as the two-phase superficial velocities j_{TP}, the two-phase superficial velocity ratio η (η $= j_G/j_L$), flow channel geometries, physical properties of the two phases, and wall wetting properties (Haase et al. [19]). The influence of these parameters can be quantified by various dimensionless numbers. In this study, the Bond number, Bo, (Bo $= \frac{(\rho_L - \rho_G)d_{it}^2 g}{\sigma_L}$), equals to 0.13; the capillary number, Ca, (Ca $= \frac{\mu_L j_{TP}}{\sigma_L}$), ranging from 3.90×10^{-4} to 3.71×10^{-3}; and the Reynolds number, Re, (Re $= \frac{\rho_L d_{it} j_{TP}}{\mu_L}$), ranging from 24 to 224. The Weber number, We, (We $= $ Ca $\times$ Re), varied from 9.17×10^{-3} to 8.30×10^{-1}. All these dimensionless numbers indicate that the interfacial forces predominated over the inertial forces and the frictional forces. It is worthwhile to characterize the effect of the centrifugal forces by means of the Dean number, De (see Eq. (2)). Whatever the conditions and configurations, the values range from 2.01 to 23.50.

Figure 4 presents typical images of stable, uniform Taylor flows observed in the ET configuration with varying superficial gas flow rates and for three liquid flow rates. It can be observed that (i) increasing gas superficial velocity or decreasing liquid superficial velocity induced greater bubble lengths; (ii) as the bubble flowed in the tube (from the outer/left to the

inner/right spirals), there was a significant increase in the bubble volume along the axial position (a similar trend was also observed in MT, not shown); and (iii) for all the operating conditions, the bubbles had a nearly flat nose and tail. This observation justifies the assumption made in the image post-processing that the bubble can be described by curved cylinders. Most Taylor bubbles observed in the literature have a hemispherical shape for the nose and tail, but some papers have reported such flat bubbles. For example, Ide et al. [32] investigated the Taylor bubble shapes in circular micro-tubes of fused silica (inner diameter, 100 μm) treated to obtain various surface wettabilities. They found that the Taylor bubble and liquid slug had a flat nose and tail in the poorly wetting tubes at low liquid flow rates but became semi-hemispherical at higher liquid flow rates as in well-wetting micro-tubes. The flat shapes reported in Kurt et al. [9] were also observed in a poorly wetting tube (i.e., FEP) with inner diameter of 1 mm. However, it should be kept in mind that these "flat" bubbles and liquid slugs in hydrophobic channels may be not exactly flat, but mildly convex in the same direction, as reported by Cubaud et al. [34]. All these findings would suggest that this uncommon curved-cylinder bubble shape (flat nose and tail) is probably due to the hydrophobic properties of the tubes (static contact angle bigger than 90°) and also closely related to the occurrence of dynamic contact angles.

Axial variation of the bubble and liquid length and bubble velocity. As displayed in Figs. 5a, 5b, whatever the operating condition and tube configuration, the bubble lengths increase linearly along the axial position while the liquid slug lengths remain constant along the axial position. Figure 6a shows that the bubble velocity also follows a linear axial increase. This suggests that the expansion effects of the gas phase are not negligible in the present 3 m long tubing but there are no effects on the liquid phase since it is incompressible. These findings are in good agreement with the trends found by Molla et al. [27], who also investigated the lengths and velocities of the gas bubbles and liquid slugs along a rectangular micro-channel (0.8 m in length, 117 μm in width and 58 μm in height). The linear axial evolution of bubble length and velocity can be expressed as below:

$$L_B(X) = F_1 X + L_{B0}, \qquad (5)$$

$$U_B(X) = F_2 X + U_{B0}, \qquad (6)$$

where F_1 and F_2 refer to the slopes of the straight lines related to bubble length and velocity with axial location; L_{B0} and U_{B0} are the initial bubble length and velocity, namely the ones immediately after the bubble forms. By using the image processing and the least squares regression method, all the slopes and initial values at $X = 0$ were calculated and are listed in Tables 2 and 3 for each operating condition. Considering that the plotted bubble lengths and velocities are within a ±5% confidence interval, it can be seen that the slope

of the bubble length, F_1, and the slope of the bubble velocity, F_2, increase with the gas superficial flow rates at a given liquid superficial flow rate.

The estimated coefficients F_1 are plotted against gas liquid flow rate ratios, η, as shown in Fig. 6b (note that η was systematically calculated at the inlet conditions in this paper). It is seen that (i) for increasing η, the slope F_1 increased strongly until η ≈ 0.8, then the growth rate slowed down, and that (ii) the difference between the ET and MT configurations remained negligible when η < 0.8, but smaller values of F_1 were obtained for the MT configuration after η ≈ 0.8. The F_1 should be correlated with the pressure drop, which is related to the unit cell length and the unit cell number, further discussed in pressure drop section.

The constants F_2 are plotted in the Appendix. They can be seen to increase linearly with η at a given j_L, at growth rates that are dependent on j_L,

Average bubble and liquid slug lengths. Figures 7a, 7b show the variation of the average dimensionless bubble length, $\langle L_B \rangle / d_{it}$, and liquid slug length, $\langle L_S \rangle / d_{it}$, as a function of η for the ET and MT configurations, respectively. The angle brackets symbol "$\langle \rangle$" is used to represent the average value. As expected, the average bubble and slug lengths over the tubing length increased linearly with η and the inverse of η respectively. Compared to most works, e.g. [19], some extremely long stable bubbles could be originally generated in the spiral shaped tube used here: the smallest and largest lengths were 3.8 and 40.4 mm for bubbles, and 2.2 and 19.6 mm for liquid slugs. The regime where the bubble length was smaller than the tube inner diameter could not be reached in this study, as it led to unsteady flows. The deviation bars in Fig. 7a are relatively large (biggest at 10%), due to the significant increase of bubble length $L_B(X)$ along the axial distance X (discussed in the previous section).

The bubble and liquid slug lengths can be predicted by the following scaling laws:

$$\frac{\langle L_B \rangle}{d_{it}} = C_3 + C_4 \frac{j_G}{j_L} = C_3 + C_4\eta, \qquad (7)$$

$$\frac{\langle L_S \rangle}{d_{it}} = C_5 + C_6 \frac{j_L}{j_G} = C_5 + C_6 \frac{1}{\eta}, \qquad (8)$$

where the constants C_3–C_6 are dependent on the configuration, the geometry of the T-junction, the fluid properties and the wetting properties [20].

The estimated coefficients are listed in Table 4. The coefficients obtained for bubble length, C_3 and C_4, are almost equal for a given configuration: $C_3 \approx C_4 \approx 4.15$ (SD = 0.4%) for ET while $C_3 \approx C_4 \approx 3.55$ (SD = 2.4%) for MT. The coefficients obtained for liquid slug lengths, C_5 and C_6, are almost equal, $C_5 \approx C_6 \approx 2.28$ (SD = 3.1%) for both configurations. At a given flow rate ratio, η , it can be seen from Fig. 7a that the average bubble lengths in the ET configuration are bigger
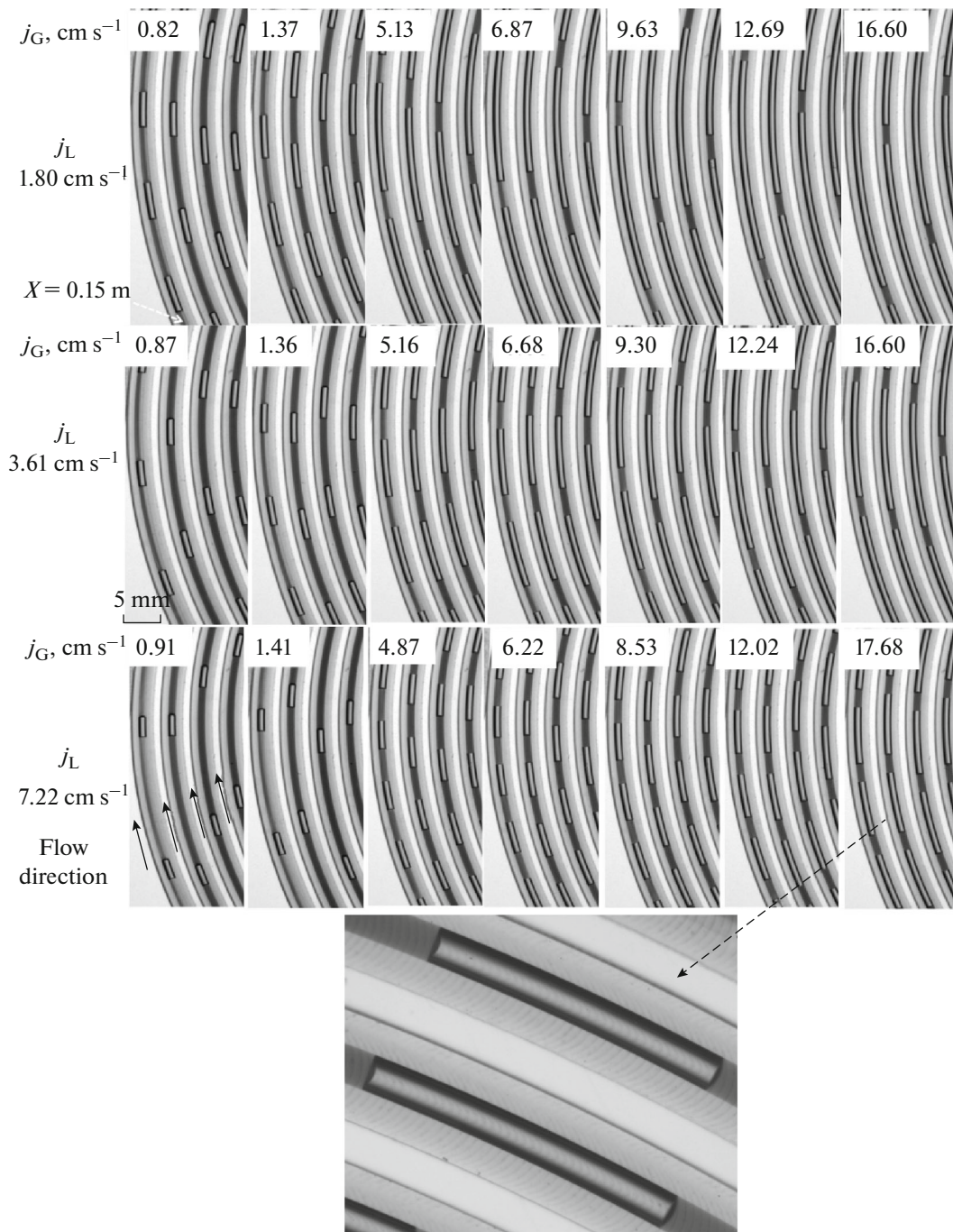
Fig. 4. Cartography of gas−liquid Taylor flows obtained for three liquid superficial velocities and various gas superficial velocities in the ET configuration and a local amplified observation of bubble shape (flat nose and tail).

than that in the MT configuration, whatever the conditions. As the Dean number ranges from 2.6 to 28.5 for ET and 3.1 to 39.2 for MT, this implies that the bubbles are shorter under higher centrifugal forces, which is consistent with the simulation results given by Kumar et al. [23].

The constant C_3 is larger than the widely-adopted coefficient for a squeezing regime proposed by Van Steijn et al. [44] and Garstecki et al. [45], which is

close to 1. This could be explained by the hydrophobic wall materials [33] and also by the increase of bubble length along the reactor. Abdelwahed et al. [33] have reported such large coefficients ($C_3 \approx C_4 \approx 3$) in the case of a train of confined bubbles inside a millimetric cylindrical T-junction device. They showed experimentally that the wetting behaviour played a significant role in the formation and motion of the bubble. In particular, they found that, in the squeezing regime,
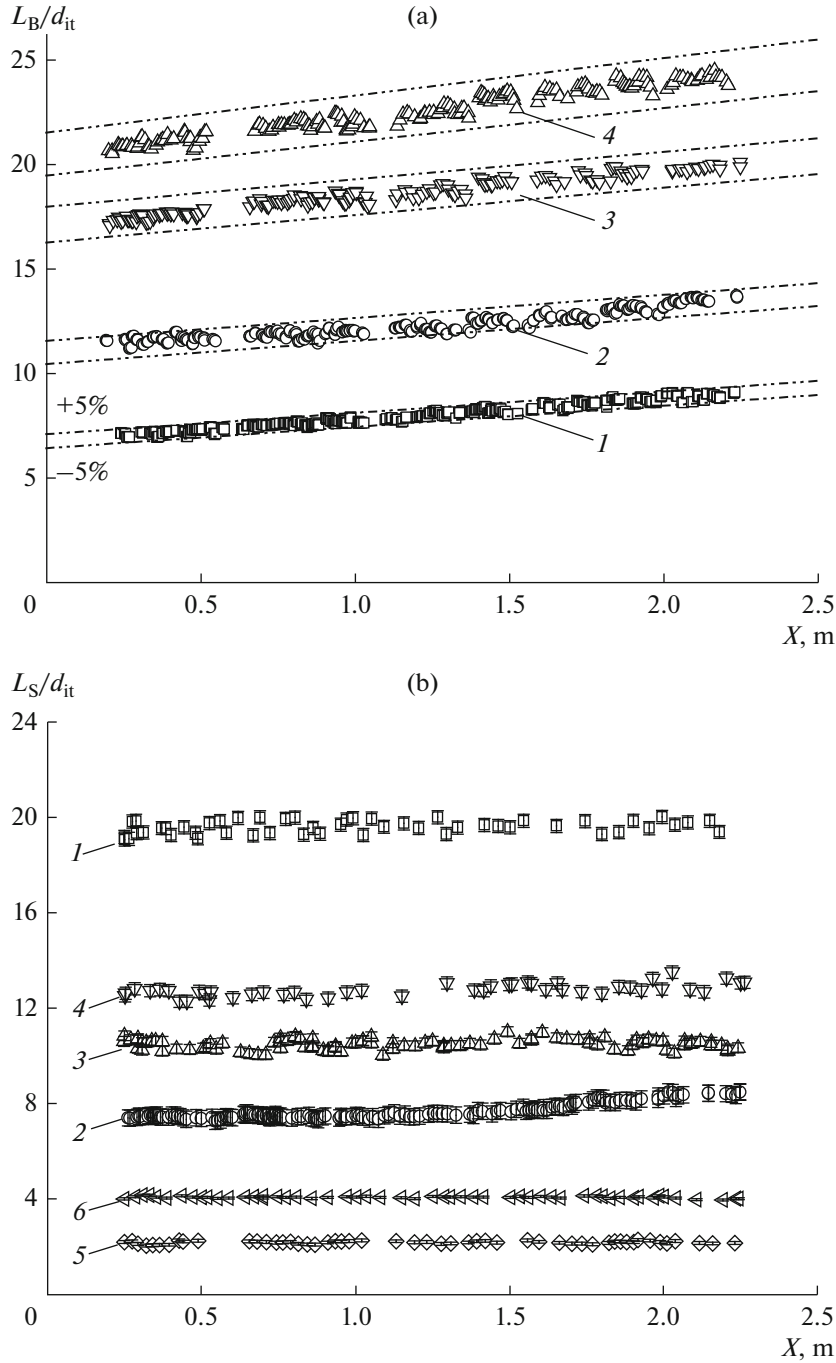
Fig. 5. (a) Dimensionless bubble length versus axial position X at $j_L = 1.80$ cm s^{-1} for the ET configuration: (*1*) $j_G = 1.37$ cm s^{-1}; (*2*) $j_G = 2.79$ cm s^{-1}; (*3*) $j_G = 5.13$ cm s^{-1}; (*4*) $j_G = 6.87$ cm s^{-1}; dash-dotted line: the ±5% confidence interval. (b) Dimensionless liquid slug length versus axial position X at different conditions: (*1*) $j_L = 7.22$ cm s^{-1}, $j_G = 0.91$ cm s^{-1}, ET; (*2*) $j_L = 7.22$ cm s^{-1}, $j_G = 3.30$ cm s^{-1}, MT; (*3*) $j_L = 3.61$ cm s^{-1}, $j_G = 1.12$ cm s^{-1}, ET; (*4*) $j_L = 3.61$ cm s^{-1}, $j_G = 0.91$ cm s^{-1}, MT; (*5*) $j_L = 1.80$ cm s^{-1}, $j_G = 16.60$ cm s^{-1}, ET; (*6*) $j_L = 1.80$ cm s^{-1}, $j_G = 3.19$ cm s^{-1}, MT.

under the same flow conditions, the gas penetrated inside the stream more easily and also more rapidly for a wetting liquid than for a non-wetting one, in which the slip condition on the wall is no longer prevalent.

These findings show that the bubble and slug lengths are governed mainly by the ratio between gas and liquid velocities, but that the wettability and centrifugal force also have noteworthy influence.
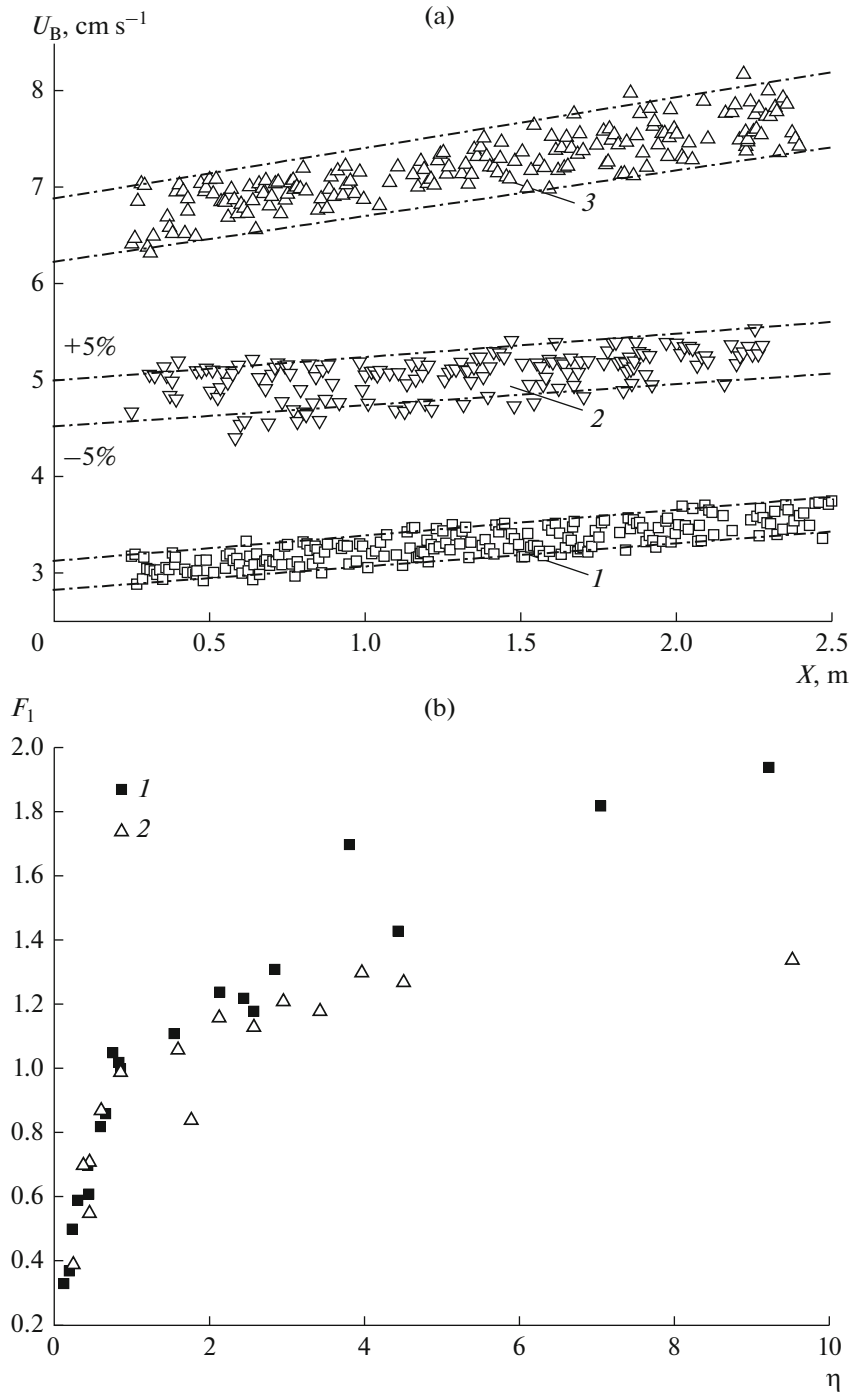
Fig. 6. (a) Bubble velocity versus axial position X at different conditions (1) $j_L = 1.80$ cm s^{-1}, $j_G = 1.37$ cm s^{-1}, ET; (2) $j_L = 1.80$ cm s^{-1}, $j_G = 3.19$ cm s^{-1}, MT; (3) $j_L = 3.61$ cm s^{-1}, $j_G = 3.04$ cm s^{-1}, ET; dash-dotted line: the $\pm 5\%$ confidence interval. (b). Linear regression coefficient F_1 versus gas–liquid flow ratio η for different configurations and superficial velocities: (1) ET, (2) MT.

Average bubble velocity. Figure 8 shows the average bubble velocity, $\langle U_B \rangle$, versus the total superficial velocity, j_{TP} (calculated at the inlet conditions), for different liquid flow rates in the ET and MT configurations. It can be seen that (i) $\langle U_B \rangle$ are higher than j_{TP} and follow a linear evolution and, (ii) the bubble velocities obtained with the ET configuration do not differ significantly from those in the MT configuration. This trend can be described using the well adapted drift flux model [46]:

$$\langle U_B \rangle = C_7 j_{TP} + C_8, \tag{9}$$
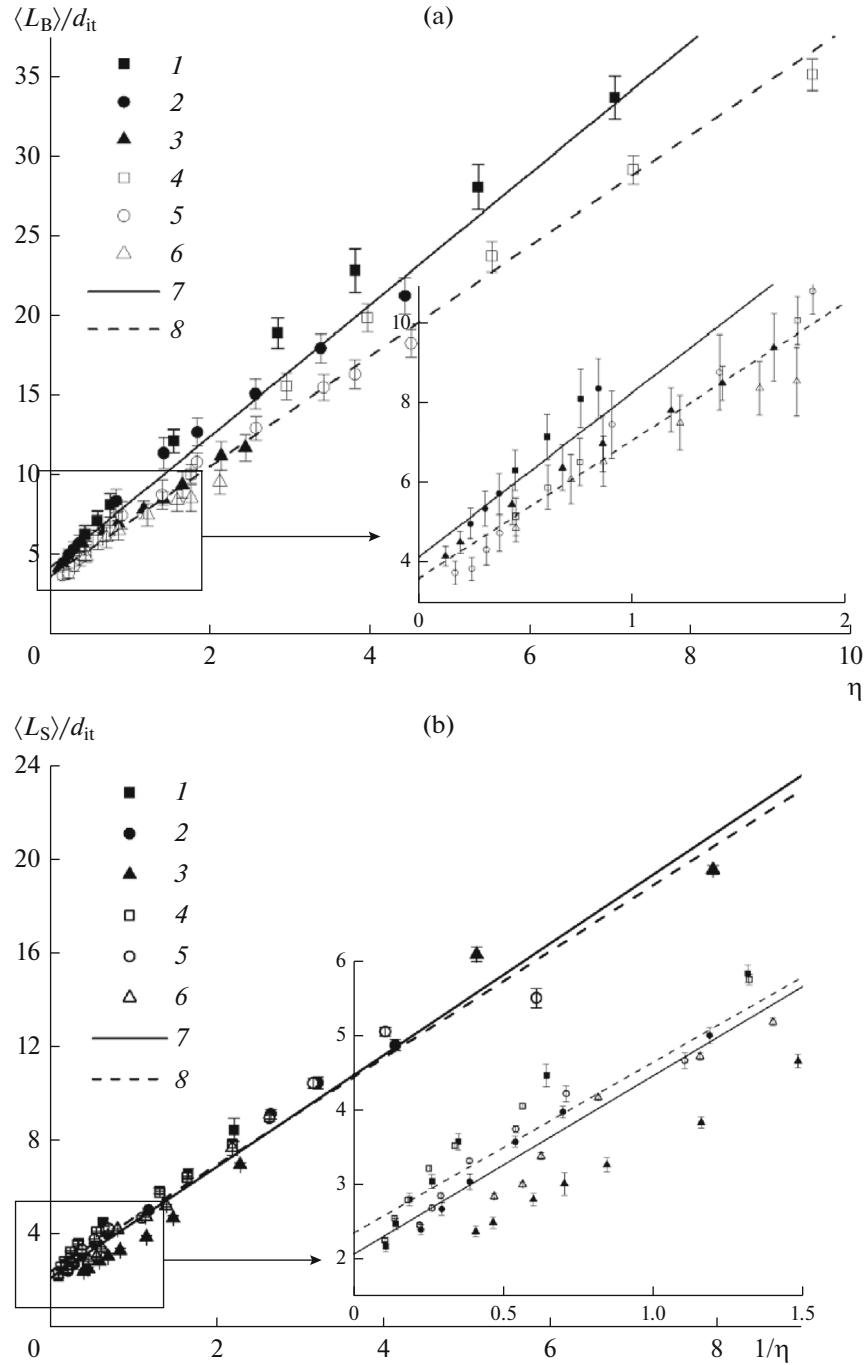
Fig. 7. (a) Average dimensionless bubble length versus flow rate ratio η for the ET configuration: (1) $j_L = 1.80$ cm s^{-1}; (2) $j_L = 3.61$ cm s^{-1}; (3) $j_L = 7.22$ cm s^{-1}; and for the MT configuration: (4) $j_L = 1.80$ cm s^{-1}; (5) $j_L = 3.61$ cm s^{-1}; (6) $j_L = 7.22$ cm s^{-1}; (7) the least squares regression law for ET, (8) the least squares regression law for MT. (b) Average dimensionless liquid slug length versus the inverse of η for the ET configuration: (1) $j_L = 1.80$ cm s^{-1}; (2) $j_L = 3.61$ cm s^{-1}; (3) $j_L = 7.22$ cm s^{-1}; and for the MT configuration: (4) $j_L = 1.80$ cm s^{-1}; (5) $j_L = 3.61$ cm s^{-1}; (6) $j_L = 7.22$ cm s^{-1}; (7) the least squares regression law for ET, (8) the least squares regression law for MT.

where C_7 and C_8 are the distribution factor and the drift velocity. For the horizontal tubes, the drift velocity is negligible, so $C_8 \approx 0$. The factor C_7 is found to be 1.17 (SD 7.3%), which is in accordance with the values encountered in the literature (varying between 0.85 and 1.38, [47]). It is interesting to note that, if the ini-

Table 4. Modelling of bubble and liquid slug lengths: empirical coefficients associated with Eqs. (6) and (7)

Configuration	Equation (6) $\dfrac{L_B}{d_{it}} = C_3 + C_4 \dfrac{j_G}{j_L}$			Equation (7) $\dfrac{L_S}{d_{it}} = C_5 + C_6 \dfrac{j_L}{j_G}$		
	C_3	C_4	SD, %	C_5	C_6	SD, %
ET	4.13	4.16	5.2	2.39	2.07	7.2
MT	3.46	3.63	4.4	2.29	2.36	4.3

tial bubble velocity, U_{B0}, (i.e. the velocity just after the bubble formation) is considered instead of $\langle U_B \rangle$, then the value of C_7 is approximately 1.

Unit cell length and relative length of the bubble. The average unit cell length was determined by the bubble and liquid slug lengths, as follows:

$$\langle L_{UC} \rangle = \langle L_S \rangle + \langle L_B \rangle. \tag{10}$$

The relative length of the bubble, $\langle \psi \rangle$, was calculated as

$$\langle \psi \rangle = \frac{\langle L_B \rangle}{\langle L_{UC} \rangle}. \tag{11}$$

The variation of the unit cell length, $\langle L_{UC} \rangle$, and the relative length of the bubble, $\langle \psi \rangle$, are plotted against η

in Figs. 9a, 9b. At fixed j_L, as j_G increases (η increasing), the length of the unit cells L_{UC} decreases to a minimum value and afterwards increases. This trend (i.e. the occurrence of a minimal value) can be explained by the fact that, when η is smaller than 0.8, the liquid slug length decreases as j_G increases, while the bubble length increases (see Tables 2 and 3).

Surprisingly, the values of $\langle \psi \rangle$ are almost identical whatever the liquid superficial velocity. They are, however, slightly higher in the ET configuration than in the MT, which is rather in agreement with the fact that the bubbles are longer in the ET configuration due to less pronounced effects of centrifugal forces and a slightly smaller pressure drop. It can also be observed that $\langle \psi \rangle$ first increases dramatically with the gas–liquid flow rate ratio, and then reaches a plateau when $\eta > 6$. This plateau corresponds to very high values of $\langle \psi \rangle$ (close to 0.95), that is to say, to very long bubbles and very small liquid slugs. When compared to the literature, such a result is quite original.

Pressure drop. In this study, the air pressure passing through the mass flow controller at the gas feeding line was measured and noted as p_r. The mass flow controller was at 4.25 m (noted as L_1), far before the T-junction point, and the inner diameter of the gas supply tube, d_G, was 0.5 mm. Considering a fully developed
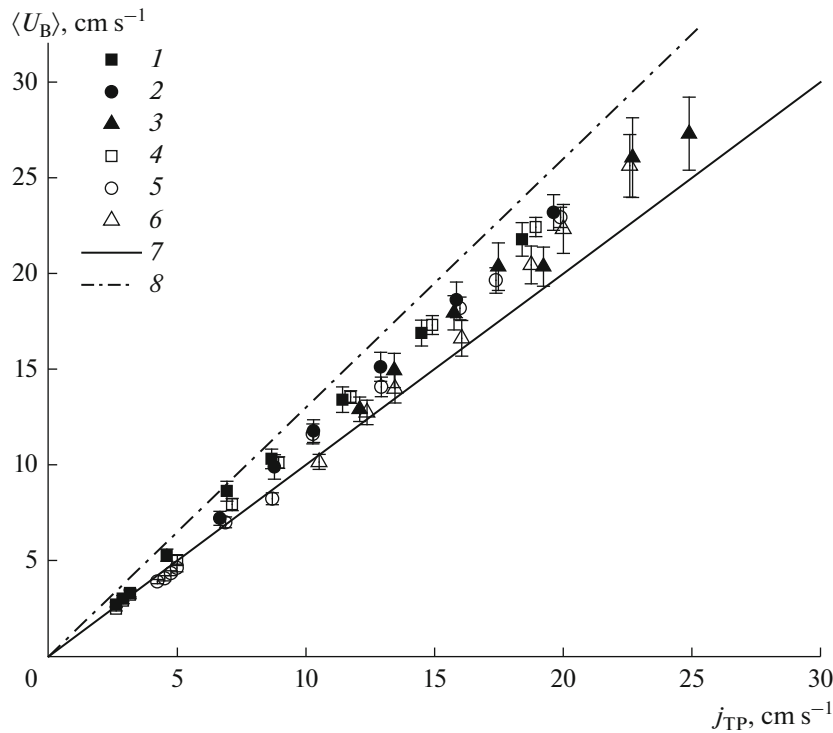
Fig. 8. Average bubble velocity versus two-phase superficial velocity for the ET configuration: (1) $j_L = 1.80$ cm s^{-1}; (2) $j_L = 3.61$ cm s^{-1}; (3) $j_L = 7.22$ cm s^{-1}; for the MT configuration: (4) $j_L = 1.80$ cm s^{-1}; (5) $j_L = 3.61$ cm s^{-1}; (6) $j_L = 7.22$ cm s^{-1}; solid line: (7) $U_B = j_{TP}$; dash-dotted line: (8) $U_B = 1.3 j_{TP}$.
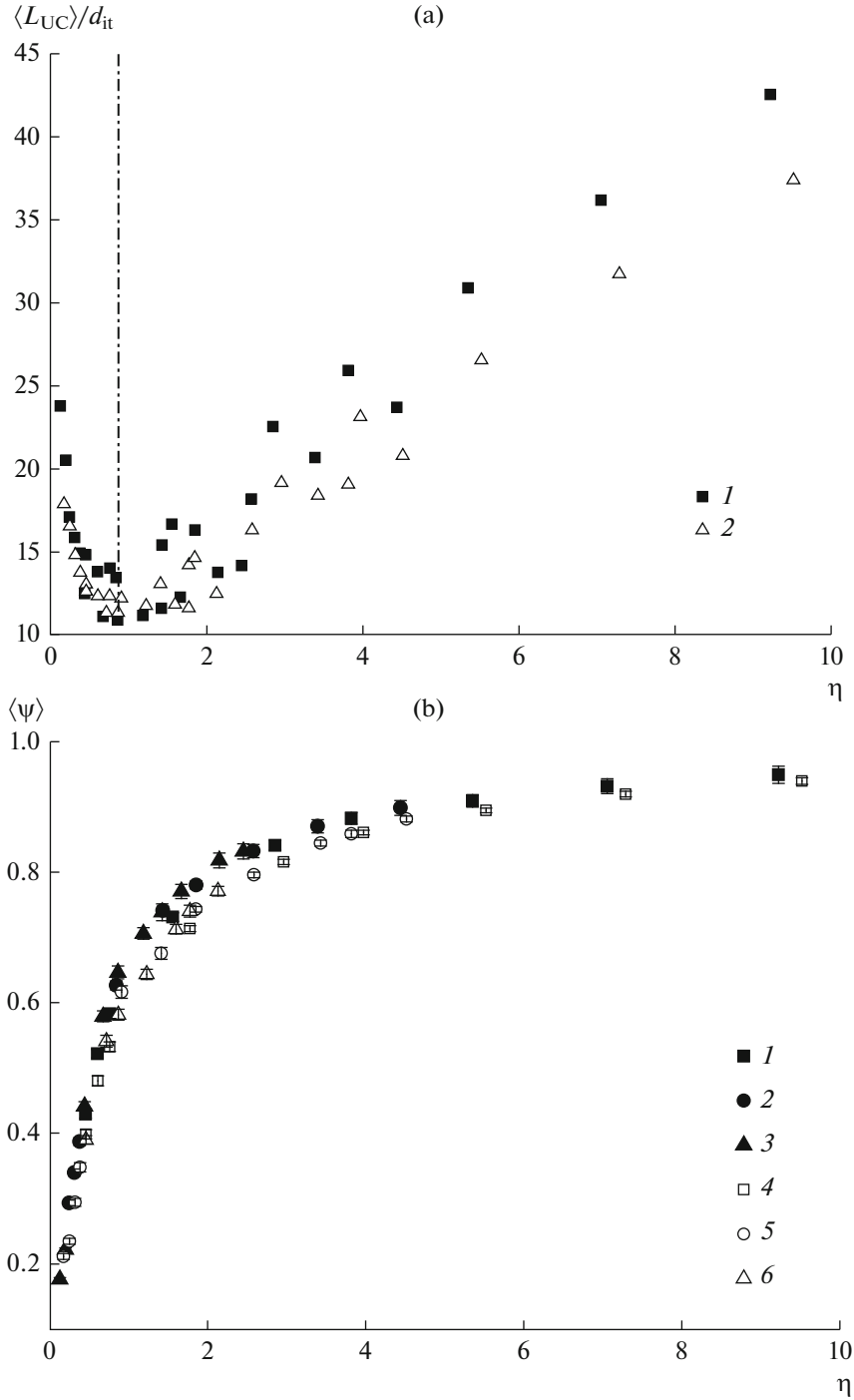
Fig. 9. (a) Average unit cell length $\langle L_{UC} \rangle$ versus flow rate ratio η: (1) ET; (2) MT; dash-dotted line: $\eta = 0.8$. (b) Average relative length of the bubble $\langle \psi \rangle$ versus η for the ET configuration: (1) $j_L = 1.80$ cm s^{-1}; (2) $j_L = 3.61$ cm s^{-1}; (3) $j_L = 7.22$ cm s^{-1}; for the MT configuration: (4) $j_L = 1.80$ cm s^{-1}; (5) $j_L = 3.61$ cm s^{-1}; (6) $j_L = 7.22$ cm s^{-1}.

Hagen–Poiseuille flow of a single phase in a tube [48], the pressure drop in the gas feed line before the T-junction, Δp_1, can be calculated for each gas flow rate.

The total pressure drop from the gas inlet (right before T-junction position) to the two-phase flow out-let, p_{r0}, can then be deduced from Δp_1 and from the absolute pressure recorded by the mass flow controller, p_r, as

$$\Delta p_{r0} = (p_r - p_{out}) - \Delta p_1. \qquad (12)$$

Table 5. Correlations for the pressure drop in the literature

Reference	Pressure drop	Frictional correlations	Frictional factors f
Vashisth et al. [49] (2007)	$\Delta p_{TP} = \Delta p_{fric}$	$\left(\dfrac{\Delta p_{TP}}{L_R}\right)_{fric} = \dfrac{f\rho_{TP}\alpha j_{TP}^2}{2d}$	$f = \dfrac{16}{Re_{TP}}\left(\dfrac{j_L}{j_G}\right)^2\left[1+9.63\left(\dfrac{Re_G}{Re_L}\right)^{0.747}Re_{TP}^{-0.019}\right]$
Kreutzer et al. [48] (2005)	$\Delta p_{TP} = \Delta p_{fric}$	$\left(\dfrac{\Delta p_{TP}}{L_R}\right)_{fric} = \dfrac{2f\rho_L\beta j_{TP}^2}{d}$	$f = \dfrac{16}{Re_{TP}}\left[1 + 0.17\dfrac{d}{L_s}\left(\dfrac{Re}{Ca}\right)^{0.33}\right]$
Bretherton et al. [43] (1961)	$\Delta p_{TP} = \Delta p_{fric}$		$f = \dfrac{16}{Re_{TP}}\left[1 + 0.465\dfrac{d}{L_s}\left(\dfrac{1}{Ca}\right)^{0.33}\right]$
Lee et al. [28] (2010)	$\Delta p_{TP} = (\Delta p_G)_{fric} + (\Delta p_L)_{fric} + \Delta p_{CAH}$	$\left(\dfrac{\Delta p_G}{L_R}\right)_{fric} = \dfrac{2f_G\rho_G\beta j_{TP}^2}{d}$ $\left(\dfrac{\Delta p_L}{L_R}\right)_{fric} = \dfrac{2f_L\rho_L(1-\beta)j_{TP}^2}{d}$	$f_G = \dfrac{16}{Re_G}$ $f_L = \dfrac{16}{Re_L}$

Therefore, the total pressure drop per unit of length $(\Delta p/L)_{r0}$ is given by the total pressure drop, Δp_{r0}, divided by the entire reactor length L_R.

Let us now consider the overall pressure drop Δp_{tot}, including the pressure loss related to the micro-reactor inlet and outlet effects, and the two-phase Taylor flow pressure drop due to the frictional and capillary forces, such that

$$\Delta p_{tot} = \Delta p_{inlet} + \Delta p_{out} + \Delta p_{TP}. \quad (13)$$

Some correlations have been proposed in the literature to calculate the two-phase Taylor flow pressure drop (Δp_{TP}): they are listed in Table 5. The associated predicted values are plotted, together with the measured pressure gradient, $(\Delta p/L)_{r0}$, in Fig. 10. Theoretically, the predicted value of $(\Delta p/L)$ should be slightly smaller than the experimental ones, $(\Delta p/L)_{r0}$, as it does not take account of the pressure losses from the inlet and outlet parts. However, the predicted pressure drops are observed to be markedly lower than the measured pressure drop when only the frictional pressure drop is considered, such as in the correlations of Bretherton et al. [43], Kreutzer et al. [48], and Vashisth et al. [49]. The correlation from Lee et al. [28] differs by the fact that it includes the capillary pressure drop. The total capillary pressure drops caused by the contact angle hysteresis (noted as CAH) in the milli-reactor can be calculated as below:

$$(\Delta p)_{CAH} = -\frac{4\sigma}{d_{it}}(\cos\theta_{RCA} - \cos\theta_{ACA})n_{UC}, \quad (14)$$

where θ_{RCA} and θ_{ACA} represent receding contact angle (RCA) and the advancing contact angle (ACA), respectively, and n_{UC} is the unit cell number ($n_{UC} = L_R/L_{UC}$). The ACA and RCA are calculated from the static contact angle, θ_S (98.7° in this study), and from

the coefficients C_9 and C_{10} taken, here, from Lee et al. [28] and equal to 0.82 and 0.118, respectively.

$$\theta_{ACA} = \cos^{-1}\left[\cos\theta_s - C_9 Ca^{C_{10}}(\cos\theta_s + 1)\right], \quad (15)$$

$$\theta_{RCA} = 2\theta_s - \theta_{ACA}. \quad (16)$$

This calculation of capillary pressure drop assumes that there is no liquid film between the Taylor bubble and the FEP material wall surface. Figure 10 clearly shows that the predictions from the correlation of Lee et al. are the closest to the measured pressure gradient. These findings would indicate that the dominant role is played by the capillary pressure drop rather than the frictional pressure drop, and that the liquid lubrication film at the walls, if it exists, is very thin.

Furthermore, the pressure drop could be estimated from the bubble volume change, considering the Ideal Gas Law (IGL) and assuming that the volume change caused by mass transfer of oxygen is negligible. From the previous variation of axial bubble length, the bubble volume can be derived from formula (5) as below:

$$V_B(X) = \Omega(F_1 X + L_{B0}), \quad (17)$$

where Ω ($\Omega = \pi d_{it}^2/4$) refers to the cross-sectional area of the inner tube. Therefore, the axial variation of pressure inside the bubble, noted as $p_B(X)$, can be estimated by

$$p_B(X) = p_{Bout}\frac{V_{Bout}}{V_B(X)}, \quad (18)$$

where p_{Bout} represents the pressure at the outlet of the micro-reactor, which is equal to atmospheric pressure, and V_{Bout} is the bubble volume at the outlet, calculated from the linear regression F_1 and L_{B0}. As the bubble volume, $V_B(X)$, increases linearly with X, the pressure will be assumed to decrease linearly with X. The initial
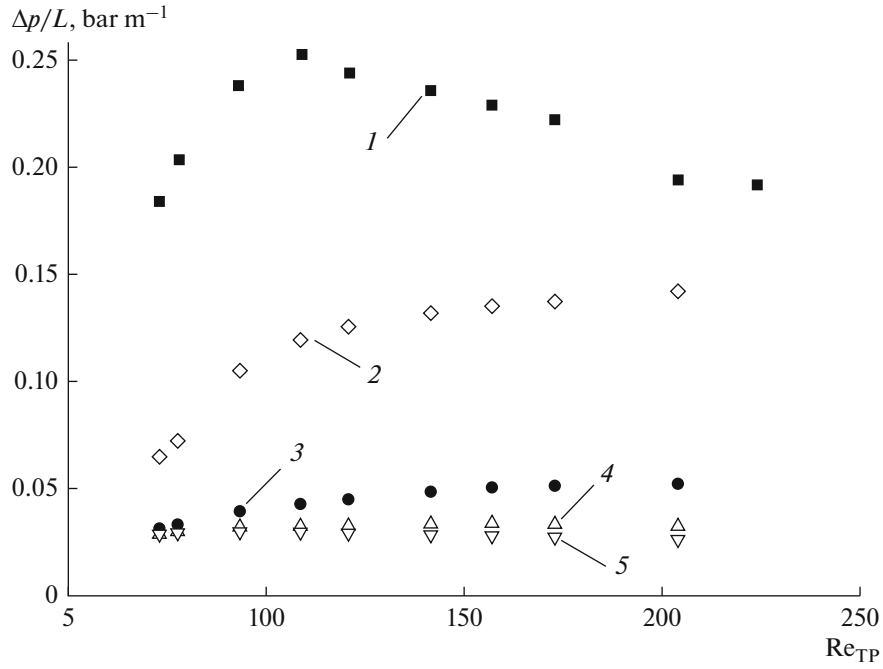
Fig. 10. Comparison of pressure drop per unit of length versus gas–liquid two-phase Reynolds number at $j_L = 7.22$ cm s^{-1} for ET: (*1*) measured experimental data; (*2*) Lee et al. (2010); (*3*) Bretherton et al. (1961); (*4*) Kreutzer et al. (2005); (*5*) Vashisth et al. (2007).

pressures inside bubbles, p_{B0}, calculated using $V_{B0} = \Omega L_{B0}$ are reported in Tables 2 and 3. Finally, the pressure gradient deduced from the bubble volume change and the Ideal Gas Law is derived from

$$(\Delta p/L)_{IGL} = (p_{B0} - p_{B_{out}})/L_R. \qquad (19)$$

Figure 11 compares the three different methods for evaluating the pressure drop by plotting it as a function of the flow rate ratio η. It can be seen that the pressure drops estimated from IGL remain smaller than the predicted ones. Here again, this is quite logical as the pressure drop estimated from IGL does not take the pressure drops related to the Taylor bubble formation (at the inlet) and to the two-phase flow separation at the outlet into account. More interestingly, the variation of $(\Delta p/L)_{IGL}$ and $(\Delta p/L)_{r0}$ presents identical trends: they first increase quickly for η < 0.8 and, after this value, decrease. From Figs. 9a and 12, one can deduce that, at this specific value η = 0.8, the unit cell length L_{UC} and the unit cell number n_{UC} achieve a maximum and a minimum respectively (n_{UC} being calculated by dividing the tube length L_R by L_{UC}). The peak in the pressure drop observed in Fig. 11 corresponds to the maximum value of the total number of moving contact lines, namely to the maximum number of unit cells. This is consistent with the conclusions of Chi et al. [28]: unlike the pressure drop in fully wetting plug flows, the energy dissipated by the moving contact lines in poorly wetting plug flows plays an important role compared to the frictional pressure dissipated by the liquid phase.

Figure 11 also shows that the pressure drops in the ET and MT configurations are very close, suggesting that an increase of centrifugal forces (from ET to MT) does not have a major impact on the pressure drop.

The figures reveal that the pressure drops predicted by Lee et al. (2010) are relatively closer to the pressure drops estimated from IGL, but the trend is not clear.

In conclusion, these findings suggest that, in poorly wetting flows, further works are required to predict the pressure drop more accurately, but they also suggest that the number of unit cells n_{UC} would be the dominant factor controlling the pressure drop, being determined by the length of the bubbles and the liquid slugs.

CONCLUSIONS

Gas–liquid two-phase Taylor flows have been investigated in a long, spiral shaped milli-reactor for a large range of curvature ratios and Reynolds numbers. The main findings are the following:

(1) Unlike those commonly observed in the literature, the Taylor bubbles were very long and had a flat nose and tail, probably due to the poorly wetting FEP tubes.

(2) The axial bubble length and velocity increased linearly with axial position, and the rates of increase were closely related to the pressure drop and centrifugal force. Along the axial position, there was no variation of the liquid slug lengths.
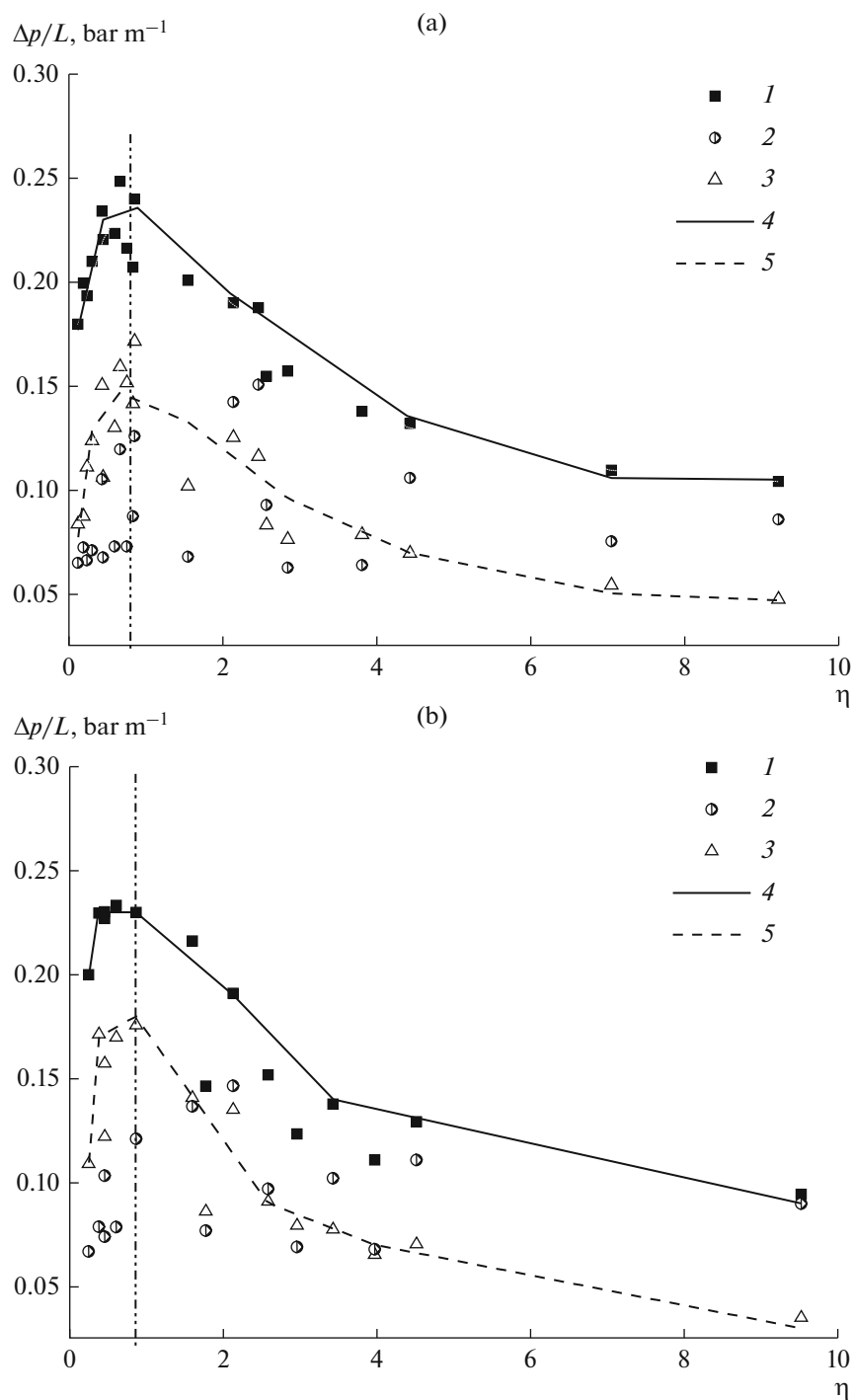
Fig. 11. Variation of pressure drops per unit of length versus gas–liquid flow rate ratio η for configuration (a) ET and (b) MT: (*1*) Experimental data; (*2*) Lee et al. (2010) (*3*) IGL; (*4*) trend line for experimental data; (*5*) trend line for IGL; dash-dotted line: η = 0.8.

(3) The formation of bubbles and liquid slugs followed the squeezing mechanism and their average lengths were mainly dependent on the gas–liquid flow rate ratio, η. Higher centrifugal force resulted in shorter Taylor bubbles and had no significant effect on liquid slug lengths.

(4) The pressure drops per unit of length estimated by IGL and the correlation of Lee et al. were compared with the measured pressure drops. In particular, the capillary pressure drop was found to be dominant when compared to the frictional pressure drop, and correlated with the total unit cell length in the reactor.
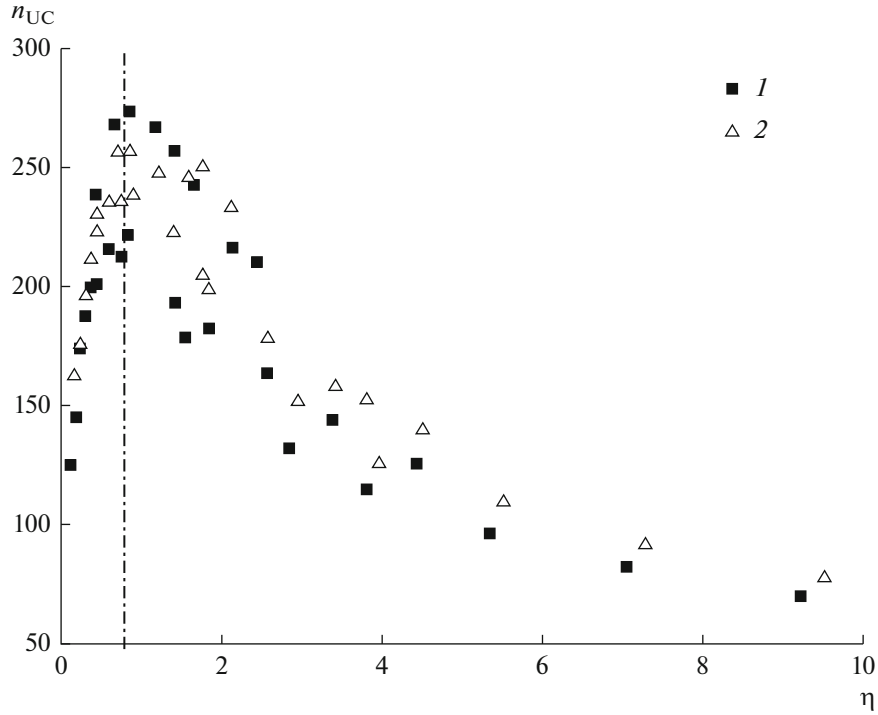
Fig. 12. Variation of unit cell number n_{UC} versus gas−liquid flow rate ratio η for different configurations (*1*) ET and (*2*) MT; dash-dotted line: η = 0.8.

All these findings give important information for understanding the characteristics of gas−liquid hydrodynamics in a long, spiral shaped tube, which could serve as a basis for implementing gas−liquid mass transfer and reaction in continuous flow reactors.

NOTATION

a	interfacial area per unit cell, m^{-1}
A	area, m
C_1	constant related to the Archimedean spiral equation (Eq. (1)), m
C_2	constant related to the Archimedean spiral equation (Eq. (1)), $m\,rad^{-1}$
$C_{3\text{-}6}$	constants related to the dimensionless length (Eq. (5)−(6)), (−)
C_7	constants related to the bubble velocity (Eq. (9)), (−)
C_8	constants related to the bubble velocity (Eq. (9)), $m\,s^{-1}$
C_{9-10}	empirical values adopted in Lee et al. (2010), (−)
D_{SR}	diameter for Archimedean spiral, m
$D_{SR,\,0}$	initial diameter for Archimedean spiral, m
d_{it}	inner diameter of the spiral tube, m
F_1	constant related to the variation of bubble length with X, (−)
F_2	constant related to the variation of bubble velocity with X, s^{-1}
g	gravitational acceleration, $m\,s^{-2}$
j_G	superficial velocity of the gas, $m\,s^{-1}$
j_L	superficial velocity of the liquid, $m\,s^{-1}$
j_{TP}	total superficial velocity for two phase flow, $m\,s^{-1}$
L_{arc}	arc length between two points of the spiral shape, m
$L_B(X)$	bubble length at a given axial position, m
$L_S(X)$	liquid slug length at a given axial position, m

$\langle L_{\mathrm{B}} \rangle$	average bubble length over the whole length of the tube, m
$\langle L_{\mathrm{S}} \rangle$	average liquid slug length over the whole length of the tube, m
L_{B0}	initial bubble length immediately after bubble formation, m
L_{SR}	sectional distance for Archimedean spiral, m
L_{R}	spiral tube length of the SR reactor, m
n	number
p_{r}	pressure recorded in the gas feed line, Pa
p_{B}	pressure inside the bubble, Pa
P_{SR}	pitch distance, m
Q	volumetric flow rate, $\mathrm{m^3\,s^{-1}}$
r	radial coordinate, m
t	time, s
$U_{\mathrm{B}}(X)$	bubble velocity at a given axial position, $\mathrm{m\,s^{-1}}$
$\langle U_{\mathrm{B}} \rangle$	average bubble velocity over the whole length of the tube, $\mathrm{m\,s^{-1}}$
$V_{\mathrm{B}}(X)$	volume of the bubble at a given axial position, $\mathrm{m^3}$
X	axial position along the spiral tube from the bubble formation point, m
x	horizontal axis in Cartesian coordinates, m
y	vertical axis in Cartesian coordinates, m
β	dynamic gas hold-up ($j_G/(j_G+j_L)$), ($-$)
ψ	relative length of the bubble ($L_{\mathrm{B}}/L_{\mathrm{UC}}$), ($-$)
η	ratio of the superficial velocities of the gas and the liquid phases, ($-$)
λ	curvature ratio, $\lambda = D_{\mathrm{SR}}/d_{\mathrm{it}}$, ($-$)
μ_{L}	dynamic viscosity of the liquid phase, Pa s
ρ_{L}	density of the liquid phase Pa s
σ_{L}	surface tension of the liquid phase, $\mathrm{N\,m^{-1}}$
θ	angular coordinate, rad
Ω	cross-sectional area of the tube, $\mathrm{m^2}$
$\mathrm{Ca} = \dfrac{\mu_L j_{TP}}{\sigma_L}$	capillary number
$\mathrm{Bo} = \dfrac{(\rho_L - \rho_G)d_{it}^2 g}{\sigma_L}$	Bond number
$\mathrm{De} = \mathrm{Re}\sqrt{1/\lambda}$	Dean number
$\mathrm{Re} = \dfrac{\rho_L d_{it} j_{TP}}{\mu_L}$	two-phase Reynolds number

SUBSCRIPTS AND SUPERSCRIPTS

B	bubble
CAH	contact angle hysteresis
fric	friction
G	gas phase
IGL	ideal gas law
it	inner diameter of the tube
L	liquid phase
out	outlet
S	liquid slug
SR	spiral shaped milli-reactor
SD	standard deviation
TP	two-phase flow
tot	total
UC	unit cell
$\langle\ \rangle$	mean value

APPENDIX

(1) Calculation of the bubble and liquid slug lengths

The bubble and liquid slug lengths are calculated based on the hypothesis that the nose and tail of the curved bubble and liquid slug are flat and that the liquid film thickness is negligible. Under these assumptions, as shown in Fig. A.1, the bubble area, A_{B}, can be deduced from the difference between the outer sector $\mathrm{OM_1M_2}$, A_{outer}, and the inner sector $\mathrm{OM_3M_4}$, A_{inner}, such as

$$A_{\mathrm{inner,B}} = \frac{\theta}{2}\left(R - \frac{d_{\mathrm{it}}}{2}\right)^2, \tag{A.1}$$

$$A_{\mathrm{outer,B}} = \frac{\theta}{2}\left(R + \frac{d_{\mathrm{it}}}{2}\right)^2 \tag{A.2}$$

$$A_{\mathrm{B}} = A_{\mathrm{outer,B}} - A_{\mathrm{inner,B}} = R d_{\mathrm{it}}\theta \tag{A.3}$$

The bubble length, L_{B}, is defined according to

$$L_B = R\theta \tag{A.4}$$

By combining Eqs. (A.3) and (A.4), one obtains

$$L_{\mathrm{B}} = \frac{A_B}{d_{\mathrm{it}}} \tag{A.5}$$

Similarly, the liquid slug length can also be deduced from the liquid slug area, A_{S}, and d_{it} as

$$L_S = \theta R = \frac{A_{\mathrm{outer,S}} - A_{\mathrm{inner,S}}}{d_{\mathrm{it}}} = \frac{A_{\mathrm{S}}}{d_{\mathrm{it}}} \tag{A.6}$$

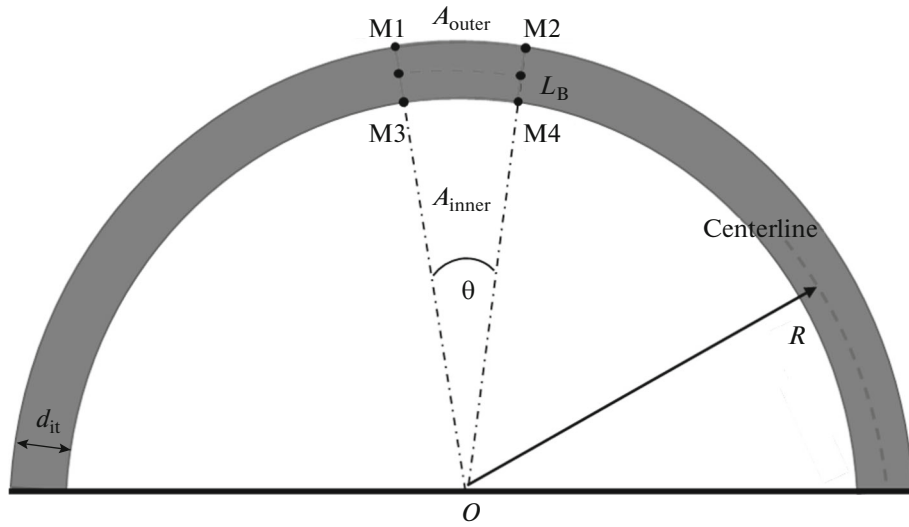(2) Variation of the constant F_2 related to the bubble velocity (Eq. (6))

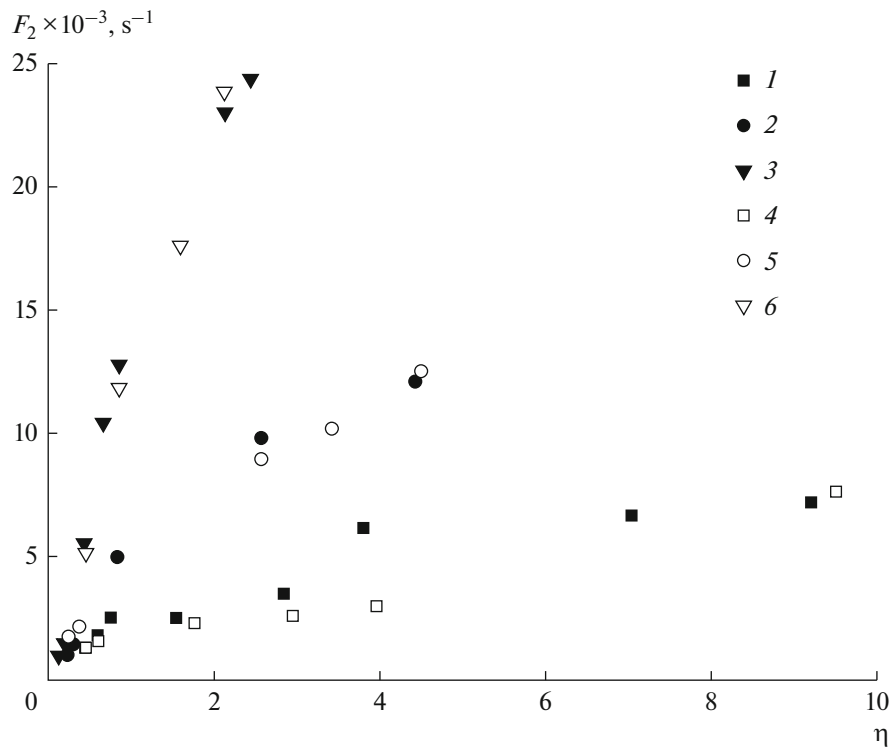**Fig. A.1.** The schematic diagram of the bubble length calculation.

Fig. A.2. Constant F_2 versus gas–liquid flow ratio for configuration ET: (*1*) $j_L = 1.80$ cm s^{-1}; (*2*) $j_L = 3.61$ cm s^{-1}; (*3*) $j_L = 7.22$ cm s^{-1}; configuration MT: (*4*) $j_L = 1.80$ cm s^{-1}; (*5*) $j_L = 3.61$ cm s^{-1}; (*6*) $j_L = 7.22$ cm s^{-1}.

REFERENCES

1. Paul, M., Strassl, F., Hoffmann, A., Hoffmann, M., Schlüter, M., and Herres-Pawlis, S., Reaction systems for bubbly flows, *Eur. J. Inorg. Chem.*, 2018, vol. 2018, nos. 20−21, p. 2101.

2. Yue, J., Multiphase flow processing in microreactors combined with heterogeneous catalysis for efficient and sustainable chemical synthesis, *Catal. Today*, 2017, vol. 308, p. 3.

3. Radjagobalou, R., Blanco, J.-F., Dechy-Cabaret, O., Oelgemöller, M., and Loubière, K., Photooxygenation in an advanced led-driven flow reactor module: Experimental investigations and modelling, *Chem. Eng. Process.*, 2018, vol. 130, p. 214.

4. Anxionnaz, Z., Cabassud, M., Gourdon, C., and Tochon, P., Heat exchanger/reactors (HEX reactors): Concepts, technologies: State-of-the-art, *Chem. Eng. Process.*, 2008, vol. 47, no. 12, p. 2029.

5. Ganapathy, H., Al-Hajri, E., and Ohadi, M., Mass transfer characteristics of gas−liquid absorption during Taylor flow in mini/microchannel reactors, *Chem. Eng. Sci.*, 2013, vol. 101, no. 14, p. 69.

6. Martínez, F.L.D., Julcour, C., Billet, A.-M., and Larachi, F., Modelling and simulations of a monolith reactor for three-phase hydrogenation reactions—Rules and recommendations for mass transfer analysis, *Catal. Today*, 2016, vol. 273, p. 121.

7. Kherbeche, A., Mei, M., Thoraval, M.-J., Hébrard, G., and Dietrich, N., Hydrodynamics and gas−liquid mass transfer around a confined sliding bubble, *Chem. Eng. J.* (in press).

8. Yang, L., Loubière, K., Dietrich, N., Men, C.L., Gourdon, C., and Hébrard, G., Local investigations on the gas−liquid mass transfer around Taylor bubbles flowing in a meandering millimetric square channel, *Chem. Eng. Sci.*, 2017, vol. 165, p. 192.

9. Kurt, S.K., Warnebold, F., Nigam, K.D.P., and Kockmann, N., gas−liquid reaction and mass transfer in microstructured coiled flow inverter, *Chem. Eng. Sci.*, 2017, vol. 169, p. 164.

10. Aillet, T., Loubiere, K., Dechy-Cabaret, O., and Prat, L., Accurate measurement of the photon flux received inside two continuous flow microphotoreactors by actinometry, *Int. J. Chem. React. Eng.*, 2014, vol. 12, no. 1, p. 257.

11. Hipolito, A., Rolland, M., Boyer, C., and De Bellefon, C., Single pellet string reactor for intensification of catalyst testing in gas/liquid/solid configuration, *Oil Gas Sci. Technol.−Revue d'IFP Energies nouvelles*, 2010, vol. 65, no. 5, p. 689.

12. Vashisth, S., Kumar, V., and Nigam, K.D., A review on the potential applications of curved geometries in process industry, *Ind. Eng. Chem. Res.*, 2008, vol. 47, no. 10, p. 3291.

13. Aillet, T., Loubière, K., Dechy-Cabaret, O., and Prat, L., Microreactors as a tool for acquiring kinetic data on photochemical reactions, *Chem. Eng. Technol.*, 2016, vol. 39, no. 1, p. 115.

14. Loubière, K., Oelgemöller, M., Aillet, T., Dechy-Cabaret, O., and Prat, L., Continuous-flow photochemistry: A need for chemical engineering, *Chem. Eng. Process.*, 2016, vol. 104, p. 120.

15. Fellouah, H., Castelain, C., El Moctar, A.O., and Peerhossaini, H., A criterion for detection of the onset of Dean instability in Newtonian fluids, *Eur. J. Mech., B*, 2006, vol. 25, no. 4, p. 505.

16. Jimenez, M., Miller, B., and Bridle, H.L., Efficient separation of small microparticles at high flowrates using spiral channels: Application to waterborne pathogens, *Chem. Eng. Sci.*, 2017, vol. 157, p. 247.

17. Fries, D.M. and von Rohr, P.R., Liquid mixing in gas−liquid two-phase flow by meandering microchannels, *Chem. Eng. Sci.*, 2009, vol. 64, no. 6, p. 1326.

18. Abiev, R., Svetlov, S., and Haase, S., Hydrodynamics and mass transfer of gas−liquid and liquid-liquid Taylor flow in micro channels: A review, *Chem. Eng. Technol.*, 2017, vol. 40, no. 11, p. 1985.

19. Haase, S., Murzin, D.Y., and Salmi, T., Review on hydrodynamics and mass transfer in minichannel wall reactors with gas−liquid Taylor flow, *Chem. Eng. Res. Des.*, 2016, vol. 113, p. 304.

20. Abadie, T., Aubin, J., Legendre, D., and Xuereb, C., Hydrodynamics of gas−liquid Taylor flow in rectangular microchannels, *Microfluid. Nanofluid.*, 2012, vol. 12, nos. 1−4, p. 355.

21. Abiev, R.S., Method for calculating the void fraction and relative length of bubbles under slug flow conditions in capillaries, *Theor. Found. Chem. Eng.*, 2010, vol. 44, no. 1, p. 86.

22. Zaloha, P., Kristal, J., Jiricny, V., Völkel, N., Xuereb, C., and Aubin, J., Characteristics of liquid slugs in gas−liquid Taylor flow in microchannels, *Chem. Eng. Sci.*, 2012, vol. 68, no. 1, p. 640.

23. Kumar, V., Vashisth, S., Hoarau, Y., and Nigam, K., Slug flow in curved microreactors: Hydrodynamic study, *Chem. Eng. Sci.*, 2007, vol. 62, no. 24, p. 7494.

24. Muradoglu, M. and Stone, H.A., Motion of large bubbles in curved channels, *J. Fluid Mech.*, 2007, vol. 570, p. 455.

25. Kawahara, A., Sadatomi, M., Matsuo, H., and Shimokawa, S., Investigation of characteristics of gas−liquid two-phase flows in a rectangular microchannel with return bends, *Proc. ASME-JSME-KSME 2011 Joint Fluids Engineering Conference*, 2011, p. 2461.

26. Ide, H., Kimura, R., Hashiguchi, H., and Kawaji, M., Effect of channel length on the gas−liquid two-phase flow phenomena in a microchannel, *Heat Transfer Eng.*, 2012, vol. 33, no. 3, p. 225.

27. Molla, S., Eskin, D., and Mostowfi, F., Pressure drop of slug flow in microchannels with increasing void fraction: Experiment and modeling, *Lab Chip*, 2011, vol. 11, no. 11, p. 1968.

28. Lee, C.Y. and Lee, S.Y., Pressure drop of two-phase dry-plug flow in round mini-channels: Effect of moving contact line, *Exp. Therm. Fluid Sci.*, 2010, vol. 34, no. 1, p. 1.

29. Choi, C., Yu, D.I., and Kim, M., Surface wettability effect on flow pattern and pressure drop in adiabatic two-phase flows in rectangular microchannels with T-junction mixer, *Exp. Therm. Fluid Sci.*, 2011, vol. 35, no. 6, p. 1086.

30. Abiev, R.S., Effect of contact-angle hysteresis on the pressure drop under slug flow conditions in minichan-

nels and microchannels, *Theor. Found. Chem. Eng.*, 2015, vol. 49, no. 4, p. 414.

31. Qu, J., Wang, Q., Li, C., Han, X., and He, Z., A simple model for Taylor flow induced contact angle hysteresis and capillary pressure inside mini/micro-scale capillary tubes, *Int. J. Heat Mass Transfer*, 2014, vol. 78, p. 1004.

32. Ide, H., Kimura, R., Inoue, K., and Kawaji, M., Effect of wetting on adiabatic gas–liquid two-phase flow in a microchannel, *Proc. ASME 6th International Conference on Nanochannels, Microchannels, and Minichannels*, 2008, p. 337.

33. Abdelwahed, M.A.B., Wielhorski, Y., Bizet, L., and Bréard, J., Characterisation of bubbles formed in a cylindrical T-shaped junction device, *Chem. Eng. Sci.*, 2012, vol. 76, p. 206.

34. Cubaud, T., Ulmanella, U., and How, C.-M., Two-phase flow in microchannels with surface modifications, *Fluid Dyn. Res.*, 2006, vol. 38, no. 11, p. 772.

35. Roudet, M., Loubiere, K., Gourdon, C., and Cabassud, M., Hydrodynamic and mass transfer in inertial gas–liquid flow regimes through straight and meandering millimetric square channels, *Chem. Eng. Sci.*, 2011, vol. 66, no. 13, p. 2974.

36. Krieger, W., Hörbelt, M., Schuster, S., Hennekes, J., and Kockmann, N., Kinetic study of leuco-indigo carmine oxidation and investigation of Taylor and Dean flow superposition in a coiled flow inverter, *Chem. Eng. Technol.*, 2019, vol. 42, no. 10, p. 1.

37. Kováts, P., Pohl, D., Thévenin, D., and Zähringer, K., Optical determination of oxygen mass transfer in a helically-coiled pipe compared to a straight horizontal tube, *Chem. Eng. Sci.*, 2018, vol. 190, p. 273.

38. Hosoda, S., Abe, S., Hosokawa, S., and Tomiyama, A., Mass transfer from a bubble in a vertical pipe, *Int. J. Heat Mass Transfer*, 2014, vol. 69, p. 215.

39. Dietrich, N., Loubière, K., Jimenez, M., Hébrard, G., and Gourdon, C., A new direct technique for visualizing and measuring gas–liquid mass transfer around bubbles moving in a straight millimetric square channel, *Chem. Eng. Sci.*, 2013, vol. 100, p. 172.

40. Dietrich, N., Wongwailikhit, K., Mei, M., Xu, F., Felis, F., Kherbeche, A., Hébrard, G., and Loubière, K., Using the "red bottle" experiment for the visualization and the fast characterization of gas–liquid mass transfer, *J. Chem. Educ.*, 2019, vol. 96, no. 5, p. 979.

41. Barajas, A. and Panton, R., The effects of contact angle on two-phase flow in capillary tubes, *Int. J. Multiphase Flow*, 1993, vol. 19, no. 2, p. 337.

42. Otsu, N., A threshold selection method from gray-level histograms, *IEEE Trans. Syst., Man, Cybern.*, 1979, vol. 9, no. 1, p. 62.

43. Bretherton, F., The motion of long bubbles in tubes, *J. Fluid Mech.*, 1961, vol. 10, no. 2, p. 166.

44. Van Steijn, V., Kreutzer, M.T., and Kleijn, C.R., μ-PIV study of the formation of segmented flow in microfluidic T-junctions, *Chem. Eng. Sci.*, 2007, vol. 62, no. 24, p. 7505.

45. Garstecki, P., Fuerstman, M.J., Stone, H.A., and Whitesides, G.M., Formation of droplets and bubbles in a microfluidic T-junction—Scaling and mechanism of break-up, *Lab Chip*, 2006, vol. 6, no. 3, p. 437.

46. Laborie, S., Cabassud, C., Durand-Bourlier, L., and Laine, J., Characterisation of gas–liquid two-phase flow inside capillaries, *Chem. Eng. Sci.*, 1999, vol. 54, no. 23, p. 5723.

47. Tsoligkas, A.N., Simmons, M.J.H., and Wood, J., Influence of orientation upon the hydrodynamics of gas–liquid flow for square channels in monolith supports, *Chem. Eng. Sci.*, 2007, vol. 62, no. 16, p. 4365.

48. Kreutzer, M.T., Kapteijn, F., Moulijn, J.A., Kleijn, C.R., and Heiszwolf, J.J., Inertial and interfacial effects on pressure drop of Taylor flow in capillaries, *AIChE J.*, 2005, vol. 51, no. 9, p. 2428.

49. Vashisth, S. and Nigam, K., Experimental investigation of pressure drop during two-phase flow in a coiled flow inverter, *Ind. Eng. Chem. Res.*, 2007, vol. 46, no. 14, p. 5043.